

# **Investigating the Interactions Between a Scanning Tunneling Microscope Tip and an Au- Coated Microcantilever**

By

© Hanin Algaidi

A thesis submitted to the  
Department of Physics and Physical Oceanography  
in partial fulfillment of the  
requirements for the degree of  
Master of Science

Department of Physics and Physical Oceanography  
Memorial University of Newfoundland

May, 2017

St. John's

Newfoundland



# Abstract

In this work we investigated the interactions between a tip used for scanning tunnelling microscopy (STM) and a Au-coated cantilever in ambient conditions. A system was constructed to position an STM tip on a Au-coated cantilever. The van der Waals, electrostatic, and capillary forces were used to model the tip-cantilever interactions. As the piezoelectric scanner adjusted the STM tip on the cantilever surface to maintain the tunnelling current set point, the magnitude of the forces changed, causing the deflection of the cantilever to vary. It was noted that the magnitude of the force was affected by the relative humidity and the tip location on the cantilever. Our experimental results showed that the van der Waals, capillary, and repulsive forces dominated the interactions and affected the stability of the cantilever during the interaction with the STM tip. It was found that an attractive force ranging between 2.4 and 27 nN acted on the cantilever when the STM was approaching toward the cantilever. The magnitudes of these forces were varied as the conditions of the experiments changed. In all cases the theoretical estimated values of the force were calculated to be well within the uncertainties. When the separation distance between the STM tip and the cantilever decreased to within a few angstroms, a repulsive force between 80- 86 nN strong was detected.

# **Acknowledgements**

I would like to express my deepest appreciation to my supervisor Dr. Luc Beaulieu for giving me the opportunity to work with him. His patience, understanding and intellect have helped facilitate my learning and the completion of this work.

Also, I would like to thank my co-supervisor Dr. Ivan Saika for his support and his valuable suggestions during my research.

I would like to thank my family who were always the source of the hope and the encouragement for me. I owe my gratitude to my father for his support, patience and for being a great father and friend for the past several years.

I will always be thankful to my friend Dr. Abdullah Alodhayb for his help and insightful comments during my study.

Finally, I would like to thank King Abdullah Scholarship Program for awarding me this scholarship and giving me the chance to get a great experience.

# Table of Contents

Abstract.....	i
Acknowledgements.....	ii
Table of Contents.....	iii
List of Figures.....	v
<b>Chapter 1 Introduction.....</b>	<b>1</b>
1.1 Microcantilever Sensors.....	1
1.1.1 Fabrication of the cantilever.....	2
1.2 Previous work.....	4
1.3 Motivation.....	5
1.4 Scope of Thesis.....	6
<b>Chapter 2 Background and Theory.....</b>	<b>7</b>
2.1 Scanning Tunnelling Microscopy.....	7
2.2 STM imaging.....	7
2.3 Tunnelling Current Theory.....	9
2.4 Literature review.....	12
2.5 Forces.....	16
2.5.1 Van der Waals force.....	16
2.5.2 Electrostatic force.....	19
2.5.3 Capillary force.....	21

2.5.4 Repulsive force .....	22
2.6 DLVO theory.....	23
2.7 Adhesive theories .....	25
2.8 The relation between the cantilever deflection and Point load position .....	28
<b>Chapter 3 Experimental setup and methods .....</b>	<b>30</b>
3.1 STM setup .....	30
3.2 Laser and PSD .....	34
3.3 Methodology .....	35
3.3.1 Sample preparation .....	35
3.3.2 SEM of STM Tips .....	35
3.3.3 Calibration of the Optical Beam Deflection System (OBDS) .....	37
3.4 Spring constant calibration.....	40
<b>Chapter 4 Results and Discussion .....</b>	<b>41</b>
4.1 Experimental procedure.....	41
4.2 Results and discussion .....	43
<b>Chapter 5 Conclusion and future work .....</b>	<b>66</b>
5.1 Conclusion .....	66
5.2 Future work.....	68
Bibliography .....	70

# List of Figures

Figure 1.1: A schematic representation of a microcantilever indicating the length  $L$ , width  $W$  and thickness  $t$ . .....2

Figure 1.2: A schematic representation of isotropic and anisotropic etching. ....2

Figure 1.3: Bulk micromachining process; a) depositing the stop layer and the device layer on the silicon wafer. b, c) depositing the photoresist layer and patterning the device layer. d, e) patterning the oxide layer and etching through the silicon wafer. ....3

Figure 1.4: STM images of a Au coated cantilever taken a) at the base, c) at 20  $\mu\text{m}$  from the base, e) at 60  $\mu\text{m}$  from the base, g) at 120  $\mu\text{m}$  from the base. Inserts b), d), f) and h) show the location of the STM tip on the cantilever (Adapted with permission from [9])..... 4

Figure 2.1: The main components of the scanning tunnelling microscope. ....8

Figure 2.2: The principal types of operations used for performing STM imaging. a) the constant current mode and b) the constant height mode. ....9

Figure 2.3: a) Schematic of two conductors with a potential barrier of height  $U$  separated by a small gap  $s$ . The gray areas represent the occupied states and the white areas represent empty states. b) Electrons from conductor ① can tunnel into conductor ② while a bias voltage  $V$  is applied. Region II represents the rise in the fermi level by  $eV$ , and  $\phi$  is the work function of conductor ①. .... 10

Figure 2.4: a) STM image taken at the base of the cantilever. b)-d) STM images taken at the free end of the cantilever with b) 1.4 V, c) 0.45V and d) 0,0036 V. e) The variation of the force as a function of the tunneling voltage for the three sites indicated in b) (Adopted with permission from reference [18])..... 13

Figure 2.5: STM image were taken on a Si cantilever with a bias of 0.7 V and a tunneling current of 0.01 nA. The green and blue dashed lines represent cross sections along similar and different scan lines (Adopted with permission from [20])..... 15

Figure 2.6: a) SEM image of a STM tip, b) and c) schematic representation indicating how the STM tip was modeled. .... 17

Figure 2.7: van der Waals force *vs.* tip-sample separation. .... 18

Figure 2.8: Electrostatic force *vs.* tip-sample separation for an applied voltage  $V = 0.5V$ ..... 20

Figure 2.9: Schematic representation of the water bridge formation between STM tip and cantilever..... 22

Figure 2.10: Interaction forces as a function of the separation distances between two charged colloidal particles. the first particle has constant charge density of  $3 \text{ mC/m}^2$  and the second particle charge density of a)  $3 \text{ mC/m}^2$  b)  $0.1 \text{ mC/m}^2$  c)  $0 \text{ mC/m}^2$  d)  $-0.5 \text{ mC/m}^2$  e)  $-3 \text{ mC/m}^2$ . (Adopted with permission from reference [39])..... 24

Figure 2.11: a) The attraction forces within the radius of the contact area are included in JKR theory. b) In DMT theory only the attraction forces without consider the contact region are included. .... 26

Figure 2.12: The cantilever deflection as a function of the point load location on the cantilever..... 29

Figure 3.1: Photographs of the STM setup including A: the STM body, B: the PSD, C: an optical microscope connected to a CCD camera, and D: an optical focuser.... 31

Figure 3.2: A photograph of the cantilever placed into a groove and held by a stainless steel clip. .... 32

Figure 3.3: a) A direct view of the STM tip and the cantilever from below. b) A front view of the STM tip on the cantilever and STM tip. c) A side view of the position of the STM tip on the cantilever.....	33
Figure 3.4: a) Photograph of the position sensitive detector (PSD). b) Schematic representation of the active area of the PSD. ....	34
Figure 3.5: a) Schematic representation of the modeled STM tip. b) SEM image of the STM tips used in this work. ....	36
Figure 3.6: Schematic representation indicating how to measure the distance between the cantilever and the PSD. (adapted with permission from Reference 50). ....	37
Figure 3.7: Schematic representation of the laser beam deflection system analysis. [Adapted with permission from Reference 51].....	38
Figure 4.1: Schematic representation showing the configuration of the major components of the experimental setup.....	42
Figure 4.2: The changes in the tunneling current (red), PSD signal (blue) and the piezo motion (green) as a function of time when the tip was approaching, engaged and withdrawing from the Au-coated cantilever surface.....	44
Figure 4.3: The cantilever deflection as a function of time in response to the STM tip. The insert is a magnified portion of the cantilever deflection showing points C and D. ....	45
Figure 4.4: The changes in the tunneling current (red), PSD signal (blue) and the piezo motion (green) as a function of time when the tip was approaching, engaged and withdrawing from the Au-coated cantilever surface.....	50
Figure 4.5: The cantilever deflection as a function of time in response to the STM tip. ....	51

Figure 4.6: The changes in the tunneling current (red), PSD signal (blue) and Piezo motion (green) in response to the approach and withdrawal of the STM tip. ....55

Figure 4.7: The cantilever deflection (in  $\mu\text{m}$ ) as a function of time in response to the process described above.....56

Figure 4.8: Measurements of the tunneling current (red), PSD signal (blue) and motion of the piezoelectric tube in the scanner (green) in response to the approach and withdrawal of the STM tip.....58

Figure 4.9: The cantilever deflection (in  $\mu\text{m}$ ) as a function of time. The insert is a magnified portion of the cantilever deflection at points B and C. ....59

Figure 4.10: The changes in the tunneling current (red), PSD signal (blue) and the piezo motion (green) as a function of time when the tip was approaching, engaged and withdrawing from the Au-coated cantilever surface.....62

Figure 4.11: The cantilever deflection as a function of time in response to the STM tip. The insert is a magnified portion of the cantilever deflection at points B and C. ....63

# Chapter 1 Introduction

## 1.1 Microcantilever Sensors

A microcantilever is a beam fixed at one end and free at the other, as shown in figure 1.1. Microcantilevers were initially used in atomic force microscopes (AFM<sup>1</sup>) as imaging probes [1]. It was later found that AFM cantilevers were sensitive to surface reactions and hence microcantilevers were investigated as potential sensors [2]. Microcantilever sensors have been used widely for various physical, chemical, and biological applications because of their numerous advantages such as high sensitivity, quick response, and low cost [2, 3]. Some examples of microcantilever sensor applications are detecting heavy metals in fresh water, DNA hybridization, antigen and antibody interactions, etc. [3, 4]. The high sensitivity of microcantilever sensors has allowed investigators to measure piconewton forces acting directly on a cantilever by monitoring the response of the cantilever to changes in surface stress.

---

<sup>1</sup> AFM is used interchangeably to mean *atomic force microscope* or *atomic force microscopy*

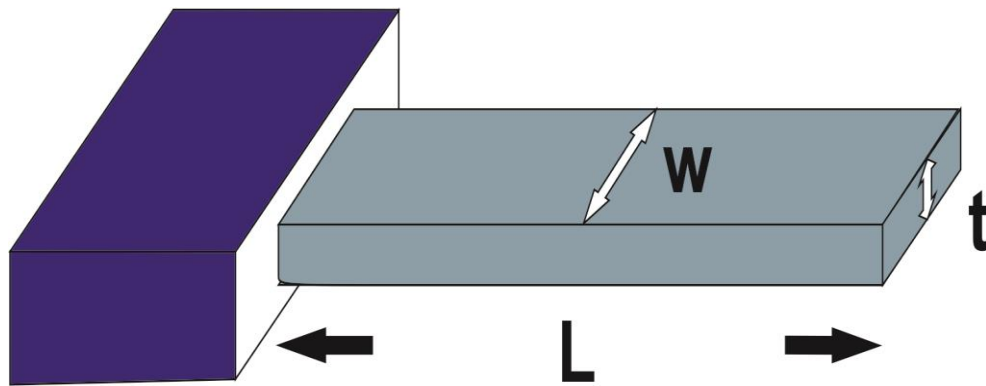


**Figure 1.1:** A schematic representation of a microcantilever indicating the length  $L$ , width  $W$  and thickness  $t$ .

### 1.1.1 Fabrication of the cantilever

Microcantilevers are fabricated predominantly from silicon, silicon nitride, piezoelectric materials, and polymers and are formed to be either rectangular or V-shaped. Microcantilevers are fabricated using bulk and/or surface micromachining techniques commonly used in the production of microelectromechanical systems (MEMS). Bulk micromachining is accomplished by using wet or dry etching, either of which can be isotropic (etch in all directions) or anisotropic (direction dependent), see figure 1.2 [5].

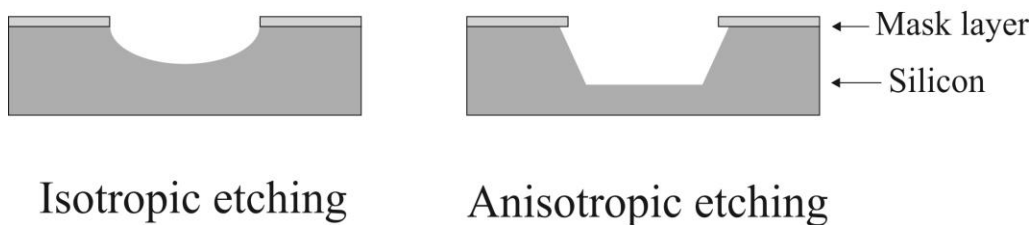


**Figure 1.2:** A schematic representation of isotropic and anisotropic etching.

Etching through the material can be controlled by either using an etch stop layer or timed etch stop where the rate of the etching is known [5]. The bulk micromachining process of the cantilever starts with depositing the material composing the cantilever, called the device layer, on top of an etch stop layer both on a silicon substrate as shown in figure 1.3 a. The device layer is patterned using a photolithography technique, where a photoresist layer is deposited to form the cantilever shape (figure 1.3 b) [6,7]. The unwanted material of the device layer is then etched away creating the cantilever shape (figure 1.3 c). The bottom of the silicon wafer is also patterned in order to form an etching mask, see figure 1.3 d [6]. As a final step in the etching process, a chemical etchant is used to etch through the silicon wafer and then the etch stop layer to release the cantilever, figure 1.3 e.

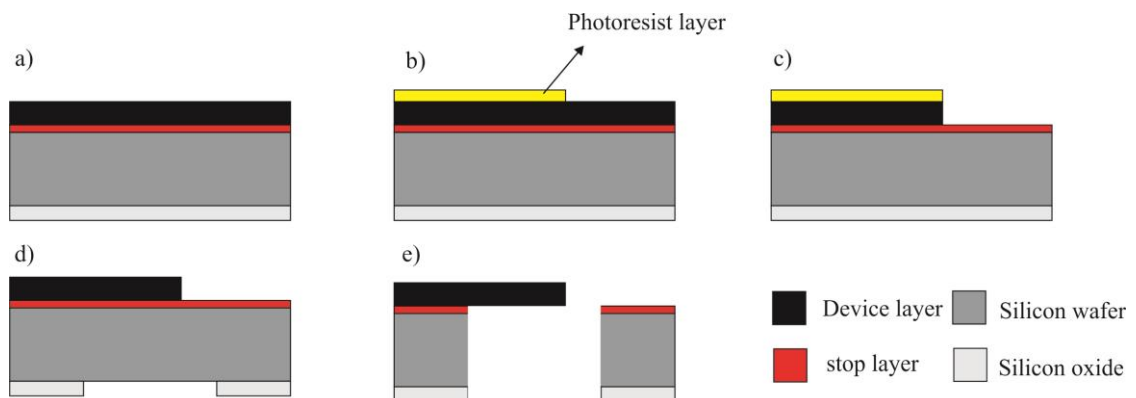


**Figure 1.3:** Bulk micromachining process; a) depositing the stop layer and the device layer on the silicon wafer. b, c) depositing the photoresist layer and patterning the device layer. d, e) patterning the oxide layer and etching through the silicon wafer.

## 1.2 Previous work

James Lacy, a former member of our group, attempted to perform *in situ* scanning tunnelling microscope (STM<sup>2</sup>) imaging of gold-coated microcantilevers. He observed that the quality of the images obtained on the cantilever quickly deteriorated as the distance of the STM tip from the cantilever base was increased (see figure 1.4). In contrast to the resolution of the image taken at the base of the cantilever (figure 1.4a), images acquired at 20, 60 and 120  $\mu\text{m}$  from the cantilever base were poor (figure 1.4c, e, g) [8].

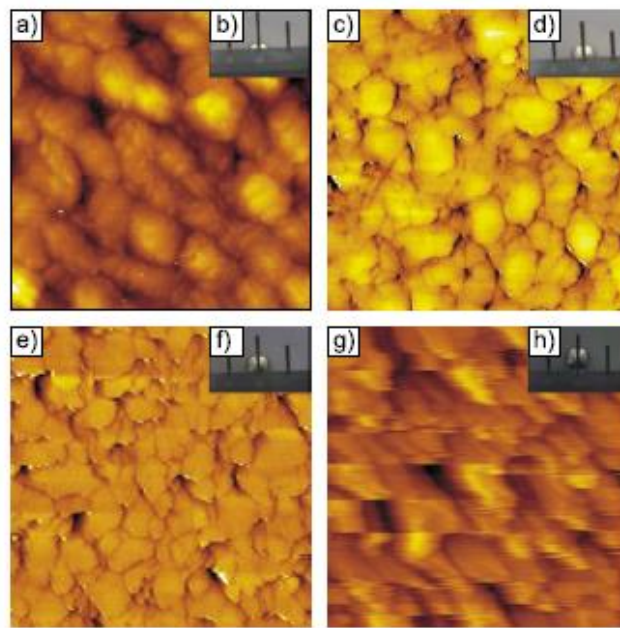


**Figure 1.4:** STM images of a Au coated cantilever taken a) at the base, c) at 20  $\mu\text{m}$  from the base, e) at 60  $\mu\text{m}$  from the base, g) at 120  $\mu\text{m}$  from the base. Inserts b), d), f) and h) show the location of the STM tip on the cantilever (Adapted with permission from [8]).

---

<sup>2</sup> STM is used interchangeably to mean *scanning tunneling microscope* or *scanning tunneling microscopy*.

He attributed the difficulty in imaging to increased vibrations that resulted from the interaction between the cantilever and the STM tip. In an effort to understand the forces behind these interactions, Lacy performed a theoretical analysis but was unable to correlate his analysis to experimental observations.

### **1.3 Motivation**

Our research group is focused on understanding the reaction dynamics which cause the deflection in cantilever sensors. Our initial goal was to image the surface of cantilever sensors during actual sensing events. Although it is possible to image the chip of the cantilever by STM while monitoring the cantilever deflection using an optical beam deflection system, our initial work attempted to image the free end of the cantilever and use the net elongation of the piezo scanner in the STM to infer the cantilever deflection. As mentioned previously, when it was observed that imaging the microcantilever was not possible due to induced mechanical vibrations, our motivation turned to understanding the forces between an STM tip and a gold-coated cantilever. In order to achieve this objective, a new experimental setup was designed and constructed to perform STM imaging on the microcantilever while using an optical beam deflection system to monitor the cantilever response to the STM imaging process.

## **1.4 Scope of Thesis**

In this work, the interaction between an STM tip and a Au-coated cantilever was investigated. In Chapter 2, a brief introduction of scanning tunnelling microscopy is given. A discussion about the type of forces that exist between an STM tip and a cantilever will also be presented. In Chapter 3, the STM setup as well as the experimental procedure used in this work is described. The experimental results obtained during the course of this work along with detailed discussions of these results are provided in Chapter 4. Lastly, a summary of this work and suggestions for the future work are presented in Chapter 5.

# Chapter 2 Background and Theory

## 2.1 Scanning Tunnelling Microscopy

The scanning tunneling microscope (STM) was invented by Binnig and Rohrer for the purpose of imaging and investigating the topography and electronic properties of surfaces [9, 10]. The main principle of operation of the STM, which belongs to the family of scanning probe microscopes (SPMs), relies on the use of quantum mechanical tunneling between a conducting stylus and the conducting surface to be imaged. In 1986, Binnig and Rohrer were awarded the Nobel Prize for their invention. Figure 2.1 shows a schematic representation of the main components of an STM. The STM consists of five major components: the tip, piezoelectric scanner, current amplifier, voltage source, and feedback loop.

## 2.2 STM imaging

An STM can be used to perform surface imaging by applying a negative bias between a conductive sample and a conductive tip brought in close proximity to the sample.

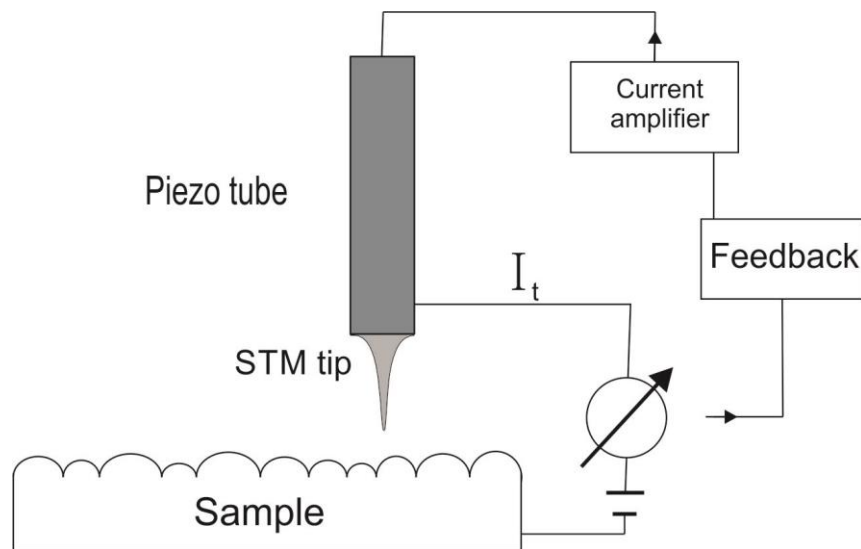


**Figure 2.1:** The main components of the scanning tunnelling microscope.

This results in the tunneling of electrons from the occupied states of the surface into the unoccupied states of the tip. The tip-sample separation is a critical factor affecting the tunneling current. Because of the exponential dependence, changing the sample-tip separation on the order of an angstrom changes the current by an order of magnitude [11].

Imaging the sample can be achieved either by keeping the height of the tip constant or the current constant. In the constant current method, the tip is made to move perpendicularly to the sample in such a way as to keep the current constant. The image is created by recording the  $(x, y, z)$  position of the tip (see figure 2.2a). In the constant height method, the height of the tip is held fixed and the tunneling current is monitored as the tip scans over the sample surface, as illustrated in figure 2.2b. The constant height method is used predominantly for performing atomic resolution imaging over a small sample area.

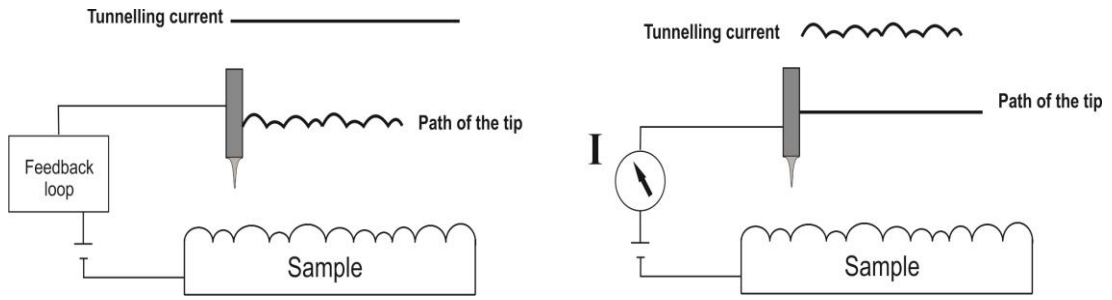


**Figure 2.2:** The principal types of operations used for performing STM imaging. a) the constant current mode and b) the constant height mode.

## 2.3 Tunnelling Current Theory

Consider a conductor ① in close proximity to a conductor ② as shown in figure 2.3a. Electrons cannot flow from one conductor to the other because the Fermi level in both conductors is the same. When a negative bias  $V$  is applied to conductor ①, the Fermi level rises by an energy  $eV$  (see figure 2.3b) proportional to the applied voltage. This allows the electrons to tunnel into the empty states in conductor ②. Assuming there is no loss of the electron's energy during the tunneling, called *elastic tunneling*, the Schrödinger equation for either conductor ① or conductor ② may be written as:

$$-\frac{\hbar^2}{2m} \frac{\partial^2}{\partial z^2} \psi(z) + U(z)\psi(z) = E\psi(z) \quad (2.1)$$

where  $m$  is the electron mass,  $U(z)$  is the potential barrier height and  $E$  is the electron energy. The solutions to the Schrödinger equation in the different regions are [12]

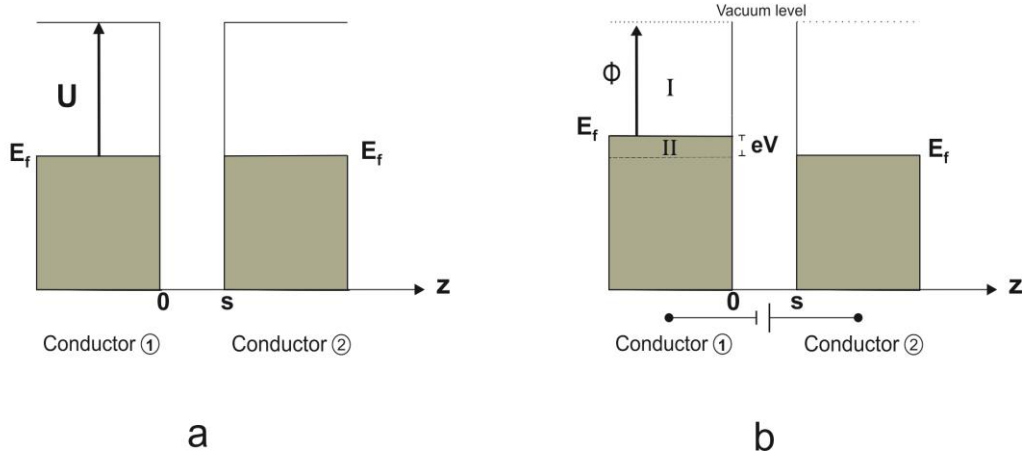


**Figure 2.3:** a) Schematic of two conductors with a potential barrier of height  $U$  separated by a small gap  $s$ . The gray areas represent the occupied states and the white areas represent empty states. b) Electrons from conductor ① can tunnel into conductor ② while a bias voltage  $V$  is applied. Region II represents the rise in the Fermi level by  $eV$ , and  $\phi$  is the work function of conductor ①.

$$\psi(z) = \begin{cases} Ae^{ikz} + Be^{-ikz} & z < 0 \\ Ce^{kz} + De^{-kz} & 0 < z < s \\ Fe^{ikz} & z > s \end{cases} \quad (2.2)$$

where  $k$  is the decay constant expressed as:

$$k = \begin{cases} \frac{(2m(E))^{1/2}}{\hbar} & z < 0 \\ \frac{(2m(U-E))^{1/2}}{\hbar} & 0 < z < s \\ \frac{(2m(E))^{1/2}}{\hbar} & z > s \end{cases} \quad (2.3)$$

Between the conductors,  $0 < z < s$ , the wave function decays exponentially. The tunneling current is the current generated as a result of the electron tunneling from

region II in conductor ① into the empty states in conductor ②. The tunneling current  $I$  is proportional to the probability of finding an electron in the gap between the two conductors, and it is given by [13]

$$I \propto \sum_{\varepsilon_n = E_F - eV}^{E_F} |\psi_n(\mathbf{0})|^2 e^{-\frac{2}{\hbar} \sqrt{2m\phi} d} \quad (2.4)$$

where  $\psi_n$  are the conductor states with energy  $\varepsilon_n$ ,  $d$  is the separation between the two conductors, and  $\phi$  is the minimum energy required to remove an electron from the metal known as the electron work function. The equation shows that the separation affects the tunneling current exponentially. In this work, it was necessary to know the separation distance between the STM tip and the cantilever. Since equation 2.4 doesn't provide the constant of proportionality, equation 2.5, for the current density,

$$J = \frac{C_1 V}{d} \sqrt{\phi} e^{(-C_2 d \sqrt{\phi})} \quad (2.5)$$

was used instead where  $C_1 = 4.74 \mu\text{A V}^{-1} \text{ \AA}^{-1} \text{ eV}^{-1/2}$ ,  $C_2 = 1.025 \text{ \AA}^{-1} \text{ eV}^{-1/2}$ ,  $\phi$  (work function of gold) = 5 eV and  $V$  is the applied voltage [14]. Therefore, the separation distance between the STM and the cantilever was obtained by dividing the magnitude of the tunneling current, obtained by our STM instrument, by the cross-sectional area of the tip and solving equation 2.5 for  $d$ .

## 2.4 Literature review

In the earlier development of the AFM, an STM tip was used to monitor the deflection of the AFM cantilever during the imaging process [15]. The STM tip was positioned on the backside of the AFM cantilever and used to monitor and record the deflection of the cantilever during the imaging process by recording the change in the tunneling current [15]. However, the sensitivity of the tunneling to contaminations on the STM tip and the cantilever along with the force exerted by the STM tip on the AFM cantilever ( $F \approx 10^{-7}$  N) made this method of detection unreliable [16].

Previous attempts have been made to study the forces occurring between an STM tip and a sample. U. Durig *et al.* (1986) studied the forces between a tungsten tip and a silver coated cantilever under UHV conditions [17]. In their work the authors used macroscopic cantilevers measuring 10 mm long, 1.5 mm wide and 0.05 mm thick [17]. The force measurements were done near the free end of the cantilever [17]. The authors reported that a repulsive force between the STM tip and the cantilever were stronger than expected [17]. The authors also observed that the surface features of the cantilever in the obtained images were affected by the tunneling voltage<sup>3</sup>  $V_t$ : *“The grooving between the flat areas and grain boundaries increases dramatically when we lower  $V_t$  from 1.4 to 0.063 V”* [17]. Compared to images taken at the free end, the images obtained at the base of the cantilever showed very little grooving, see figure 2.4 [17]. Imaging the cantilever was done for three different tunneling voltages (1.4 V, 0.45V, 0,0036 V) [17].

---

<sup>3</sup> Tunneling voltage refers to the voltage applied between the STM tip and the sample.

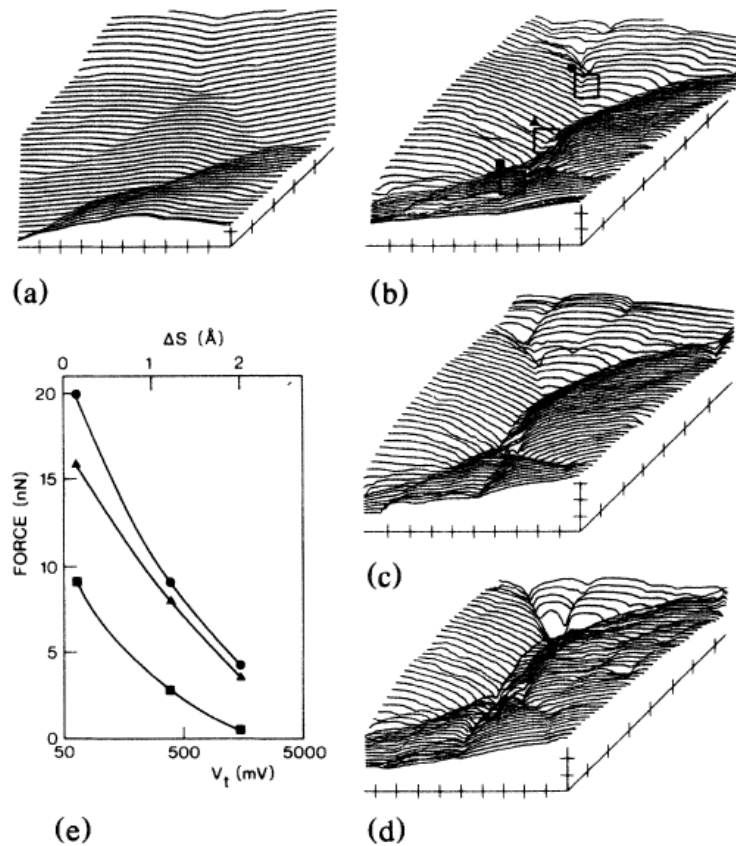


**Figure 2.4:** a) STM image taken at the base of the cantilever. b)-d) STM images taken at the free end of the cantilever with b) 1.4 V, c) 0.45V and d) 0,0036 V. e) The variation of the force as a function of the tunneling voltage for the three sites indicated in b) (Adopted with permission from reference [17]).

The value of the force was found to be a function of the tunnel voltage for the three sites indicated in figure 2.4b is shown in figure 2.4e. The graph shows the force increased by 10-15 nN at the three sites from decreasing the tunneling voltage from 1.4V to 0.0036V. Even though they were able to image at the free end of the cantilever, the large size of the cantilevers they used would not give them the opportunity to detect any small forces that that could affect the cantilever deflection.

Using micrometer-sized cantilevers would have allowed the authors to obtain more insight into the interactions between the STM tip and the cantilever beam.

In a separate study Bach *et al.* investigated the stress relief occurring during the reconstruction of Au coated cantilevers as a result of the injection of a HClO<sub>4</sub> solution during an electrochemical process [18]. In their work, the authors used STM imaging to observe the structural changes of the Au film and as a method to measure the changes in surface stress. The obtained images showed larger noise than usual which they attributed to the fact that their cantilever chip was not held securely enough [18]. The authors did not consider that the noise that was observed came from the natural thermal oscillation of the cantilever or to the interactions between the STM tip and the cantilever.

Tetsuya Narushima *et al.* (2007) attempted to investigate the origin of surface stress occurring during the changes in the atomic structure of the cantilever surface due to adsorption of Br<sub>2</sub> on a Si cantilever [19]. Their measurements were performed by STM in UHV using large cantilevers, 50 mm long, 10 mm wide and 0.5 mm thick were used to overcome the problem of the cantilever oscillation [19]. The observation of the atomic structure of the cantilever surface was acquired at the midpoint along the length of the cantilever [19]. The deflection of the cantilever as a result of the changing surface stress was measured by using the capacitive detection method, [19]. This method consists of two adjacent parallel plates forming a capacitor with the cantilever beam acting as one of the capacitor plates [19, 20]. As the cantilever deflects the capacitance between the cantilever and the reference electrode can be monitored and then the cantilever deflection can be measured [19,20]. Despite being

able to measure the deflection of the cantilever, the deflection due the interaction between the STM tip and the sample was not considered in their results. The effect of the electrical noise, the natural thermal oscillation of the cantilever, or a bad STM tip on the resolution of the obtained images were only considered, see figure 2.5. In addition, unlike using microcantilevers, using large cantilevers do not allow one to detect small forces that act on the cantilever.

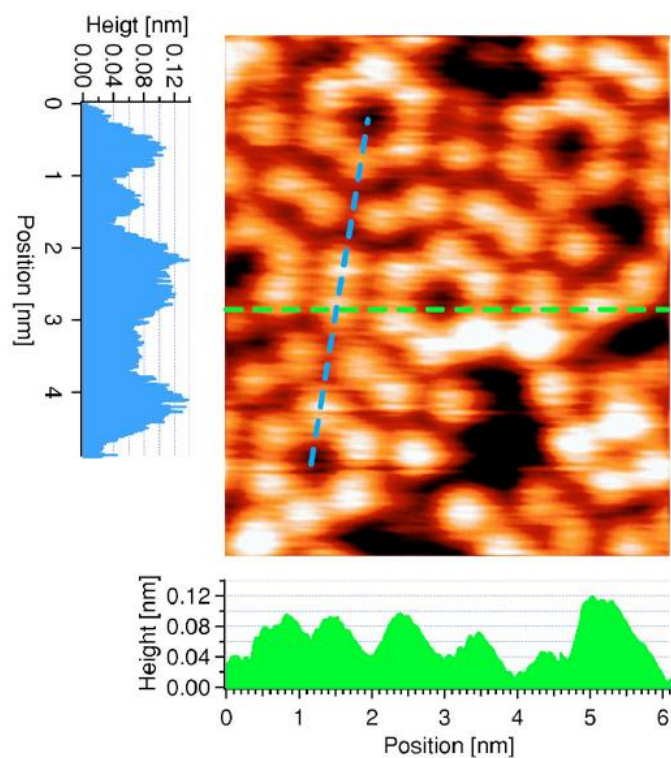


**Figure 2.5:** STM image were taken on a Si cantilever with a bias of 0.7 V and a tunneling current of 0.01 nA. The green dashed line represents a cross section along the scan line. The noise fluctuation of different scan line is represented by the blue dashed line (Adapted with permission from [19]).

## 2.5 Forces

As previously mentioned, performing STM imaging along the cantilever causes the cantilever to oscillate. Due to the interactions between the STM tip and the surface of the cantilever, the resolution of the obtained images gradually deteriorates as the distance of the STM tip from the cantilever base increases. Various types of forces exist between the tip and the sample which can be categorized based on their range of influence. The main forces influencing this system are van der Waals, electrostatic, capillary, and repulsive force<sup>4</sup>. Therefore, the total force of interaction between the STM tip and the cantilever surface was calculated by considering the van der Waals, electrostatic, capillary, and repulsive force [21, 22, 23].

### 2.5.1 Van der Waals force

An attractive van der Waals (VDW) force appears when objects are positioned close to each other. This force arises from fluctuating dipoles which are induced from the instantaneous position of the electrons in the atoms of the adjacent objects. To characterize the van der Waals force the STM tip needed to be fully characterized and the tip-surface separation  $z$  needed to be known. As shown in figure 2.6, the tip consists of two portions that can both be described as cones. The end of the larger upper cone is embedded into the lower smaller cone. Since the VDW force decays quickly with large separation, only the lower portion of the tip was considered in the

---

<sup>4</sup>Since the tips and the samples used in this work are not ferromagnetic, the magnetic force is not considered.

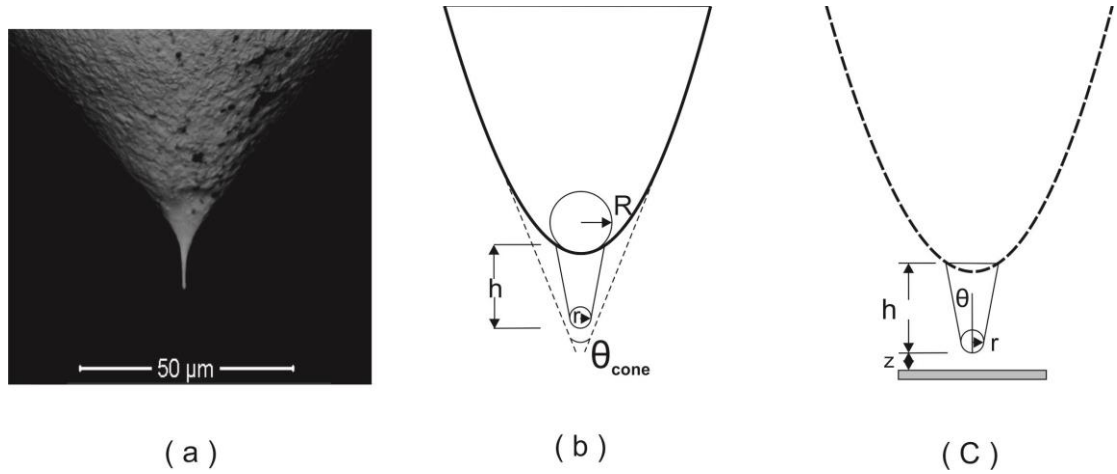


**Figure 2.6:** a) SEM image of a STM tip, b) and c) schematic representation indicating how the STM tip was modeled.

determination of the VDW force. The lower cone was characterized with the geometric parameters  $r$ ,  $h$  and  $\theta$ , where  $r$  is the radius of the sphere,  $h$  is the height of the cone, and  $\theta$  is the half angle of the cone. The VDW interaction between the tip and the surface of the cantilever was described by [24]:

$$F_{VDW}(z) = -\frac{H}{6} \left[ \frac{r}{z^2} + \frac{(\tan \theta)^2}{z + r(1 - \sin \theta)} - \frac{r(1 - \sin \theta)}{z(z + r(1 - \sin \theta))} \right] \quad (2.6)$$

where  $H$  is the non-retarded Hamaker constant which represents the van der Waals interaction strength between macroscopic bodies. The value of the Hamaker constant of two different materials 1 and 2 interacting across a medium 3 is given by

$$H_{123} = (\sqrt{H_{11}} - \sqrt{H_{33}}) * (\sqrt{H_{22}} - \sqrt{H_{33}}) \quad (2.7)$$

where  $H_{11}$ ,  $H_{22}$  and  $H_{33}$  are the Hamaker constants of material 1, 2 and 3 respectively [25]. The value of the Hamaker constant for gold is  $40 \times 10^{-20}$  J. Since the exact value for the tip material  $\text{Pt}_{0.8}\text{Ir}_{0.2}$  is not available, the Hamaker constant for platinum  $H = 20$

$\times 10^{-20}$  J was used instead [26]. In order to determine the magnitude of the van der Waals force when the STM tip was within a few nanometers of the cantilever, the water film on the cantilever should be considered as the medium of the interactions since the experiments were conducted in ambient condition. By using the Hamaker constant of water ( $H = 3.7 \times 10^{-20}$  J), the Hamaker constant for the STM tip/gold coated cantilever interacting through a water film was found to be  $H = 11.21 \times 10^{-20}$  J. Figure 2.7 shows the van der Waals force for a tip with a radius of 270 nm, the negative sign means the force is attractive. As the separation distance between the tip and the sample surface decreases, the van der Waals force increases. The value of the van der Waals force at a separation of 50 Å and 10 Å are 0.49 nN and 12 nN respectively.

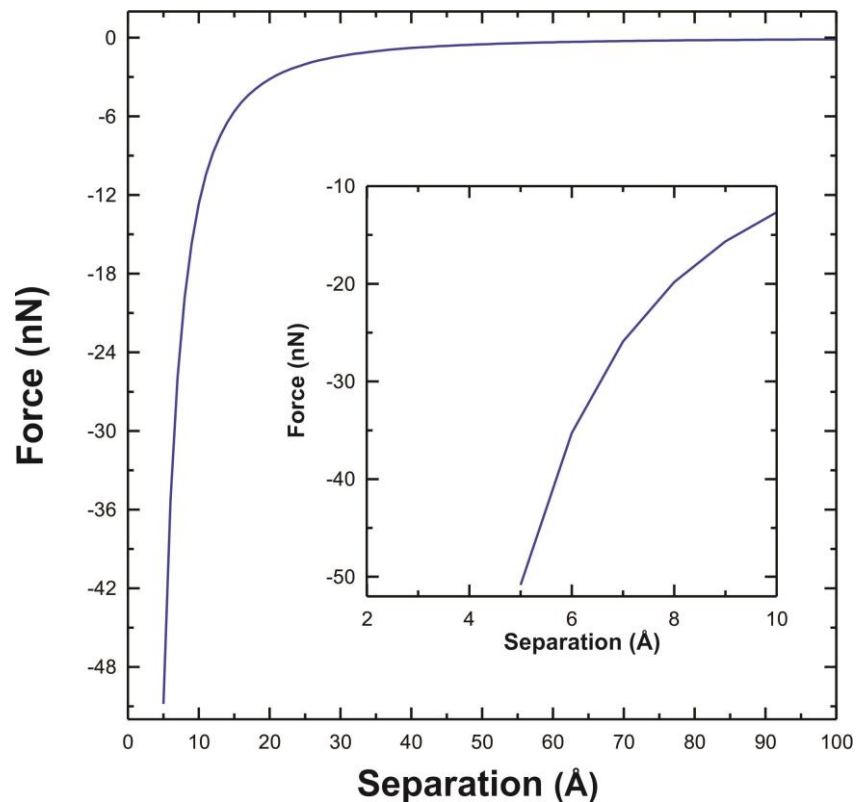


**Figure 2.7:** van der Waals force vs. tip-sample separation.

## 2.5.2 Electrostatic force

During STM imaging, a voltage bias is applied between the STM tip and the cantilever. Therefore, electrostatic interactions are present. Under a constant voltage bias, the tip and the surface of the cantilever form a capacitor. For a small tip-surface separation (i.e.  $z$  (separation)  $\ll r$  (tip radius)), the electrical force between the upper cone of the tip and the sample was found by J. Colechero *et al.*, and it is given by [27]

$$F_{el}(z) = \frac{-\pi\epsilon_0 V^2}{1 + f(\theta_{cone}) \left(\frac{z}{R}\right)} \left(\frac{R + \frac{z}{2}}{R - 2z}\right)^2 \left[ \frac{R - 2z}{z \left[1 + 2 (\tan \theta_{cone})^2 \left(\frac{z}{R}\right)\right]} + 2 \ln \left[ \frac{4z}{2z + R + (R - 2z) \cos \theta_{cone}} \right] \right] \quad (2.8)$$

with

$$f(\theta_{parabola}) = \frac{\ln \left[ \frac{1}{\sin(\theta_{cone}/2)} \right]}{\left[ (1 - (\sin \theta_{cone}/2))(3 + (\sin \theta_{cone}/2)) \right]} \quad (2.9)$$

In equations 2.8 and 2.9,  $R$  and  $\theta_{cone}$  are the radius and opening angle of the upper cone respectively as shown in figure 2.6. The electrostatics force induced from the lower cone of the tip is given by [28]

$$F_{el}(z) = -\pi\epsilon_0 V^2 K^2 \left[ \ln \left( \frac{h}{z + r(1 - \sin \theta)} \right) - 1 + \frac{r \frac{(\cos \theta)^2}{\sin \theta}}{z + r(1 - \sin \theta)} \right] - \pi\epsilon_0 V^2 \frac{r^2 (1 - \sin \theta)}{z(z + r(1 - \sin \theta))} \quad (2.10)$$

with

$$K = \frac{1}{\ln(\tan\theta/2)} \quad (2.11)$$

In equation 2.10,  $h$  is the lower cone height,  $\theta$  is the half angle of the lower cone and  $\epsilon_0$  is the vacuum permittivity. Similar to the van der Waals force, the equations show that the electrostatic force is influenced by the geometry of the tip and the tip/sample separation  $z$ . Figure 2.8 shows the electrostatic force as a function of the sample-tip separation. The magnitude of the electrostatic force at a separation of 10 Å and with an applied voltage of 0.5 V is  $1.8 \times 10^{-9}$  N. In contrast to the van der Waals force, the electrostatic force is significantly weaker.

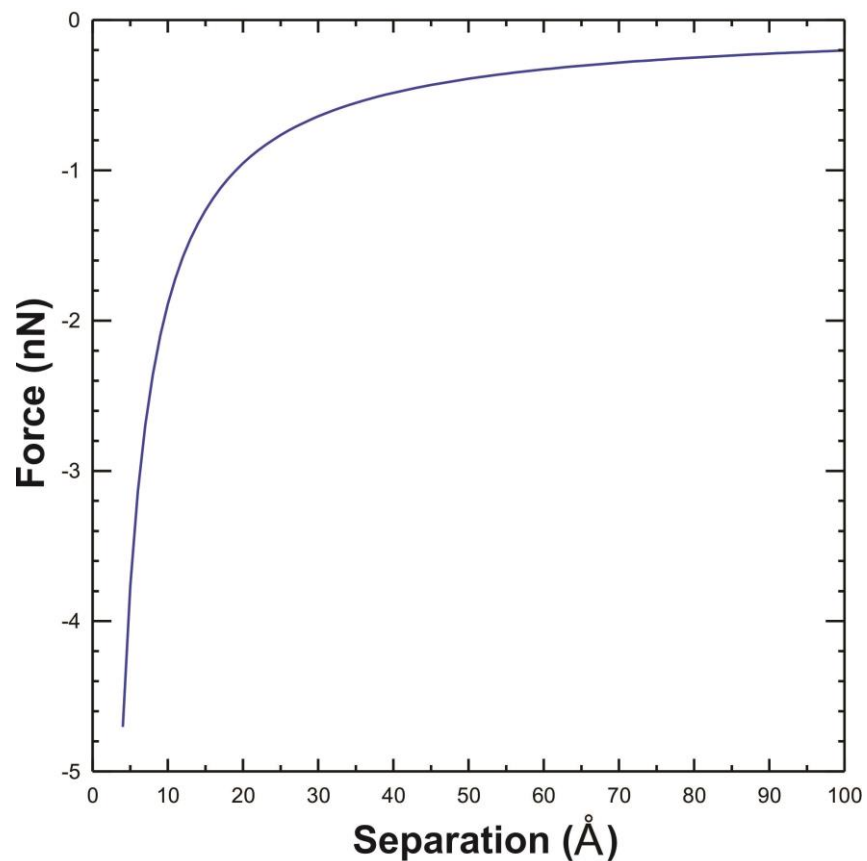


**Figure 2.8:** Electrostatic force vs. tip-sample separation for an applied voltage  $V = 0.5V$ .

### 2.5.3 Capillary force

When the STM is operated under ambient conditions, a thin layer of water grows on the substrate surface which gives rise to a capillary force. The capillary force increases the load which acts on the substrate and is estimated to be in the range of 10 - 100 nN [20]. Several factors affect the strength of the capillary force such as the relative humidity. At high temperature and low relative humidity condition, the water layer thickness formed between the tip and the surface is minimal. When the STM tip is within 8 nm of the sample, a water bridge forms between the two objects creating a capillary force [29]. Typically, this force is characterized using equation 2.12

$$F = 4\pi R\gamma \cos \alpha / (1 + D/d) \quad (2.12)$$

where  $R$  is the radius of the tip,  $\gamma$  is the surface tension of the water,  $\alpha$  is the contact angle,  $d$  is the tip-sample separation distance, and  $D$  is water height on the tip. Since the contact angle could not be determined in our experiments, a time-dependent capillary force equation was used instead [30] given by:

$$F_{cap}(t) \approx \gamma d \frac{1}{\ln\left(\frac{P_0}{P}\right)} \ln\left(\frac{t}{t_0}\right) \quad (2.13)$$

where  $d$  is the separation distance,  $P_0/P$  is the relative humidity,  $t_0$  is the condensation time for a monolayer (25  $\mu$ s) and  $t$  is the time needed to condense a water bridge between the STM tip and the cantilever [31]. Equation 2.13 describes the capillary force only during and after the formation of the condensation bridge between two surfaces but does not apply when the two surfaces are in physical contact.

When the STM tip is in close proximity to the water surface, the water bridge will start to form and the cantilever will subsequently start to deflect upwards toward the tip as illustrated in figure 2.9. In order to determine the time of the water bridge formation between the STM tip and the cantilever, the time of the snap-to-contact deflection obtained in the experiment is used as an approximation of  $t$ .

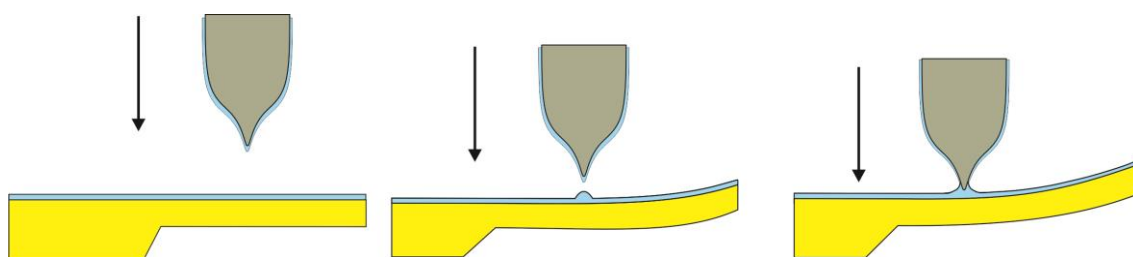


**Figure 2.9:** Schematic representation of the water bridge formation between STM tip and cantilever.

## 2.5.4 Repulsive force

The interactions between an STM tip and the surface of a sample are influenced by the tip-sample separation distance. When the tip gets closer to the sample, a reduction of the attractive forces is observed [23]. As the separation distance decreases ( $< 10$  Å), the electron wave function of the cantilever and the tip begin to overlap, and a short range repulsive force on the order of 10 - 1000 nN starts to dominate. This force is responsible for preventing two atoms from collapsing together by their mutual attractive force [21, 32, 33]. Unfortunately, there is no analytical equation that we were able to use to model the repulsive force between the STM tip and the Au-coated cantilever. In this work the repulsive force was inferred by the fact that in equilibrium

the sum of the van der Waals, capillary, cantilever force<sup>5</sup> and the repulsive force should be equal to zero. Therefore, the magnitude of the repulsive force was estimated to be equivalent to the sum of the van der Waals, capillary and cantilever force.

## **2.6 DLVO theory**

As the experiments were conducted in ambient conditions, the condensation of a water film on the cantilever surface was taken into account. The interactions between two charged surfaces in liquids can be explained by the Derjaguin, Landau, Verwey, and Overbeek (DLVO) theory [34, 35, 36]. The theory combines the electrostatic double layer, the van der Waals and structural intermolecular forces [35, 36]. The electrostatic double layer forces appear at solid-liquid interfaces when an unequal ion distribution occurs between the phases [35, 36]. A layer of charges will form on one side of the interface and another layer of opposite charges on the other side [35, 36]. The two parallel layers result in a potential across the interface. The DLVO forces decay exponentially, and the decay length is called the Debye length which can be determined by knowing the salt concentration [37].

The type of the DLVO interactions between two charged surfaces approaching each other are highly affected by the sign of the charges and the charge density as can be seen in figure 2.10 [38]. The figure illustrates the interaction profiles of two similarly charged, charged-neutral and oppositely charged surfaces with the boundary conditions of charged colloidal systems; constant charge CC (insulator), charge regulation CR (ionizable groups at the surface), and constant potential CP (conducting

---

<sup>5</sup> The reaction of the cantilever in response to the external forces acting on it.

electrode) [38, 39]. The interactions presented in the graphs are the forces between two particles, where the charge density of the first particle is constant ( $3 \text{ mC/m}^2$ ), and the charge density of the second particle is varied from  $3 \text{ mC/m}^2$  to  $-3 \text{ mC/m}^2$ . In the case where the two particles are similarly charged and have the same charge density ( $3 \text{ mC/m}^2$ ), the repulsive double layer force dominates at large separation

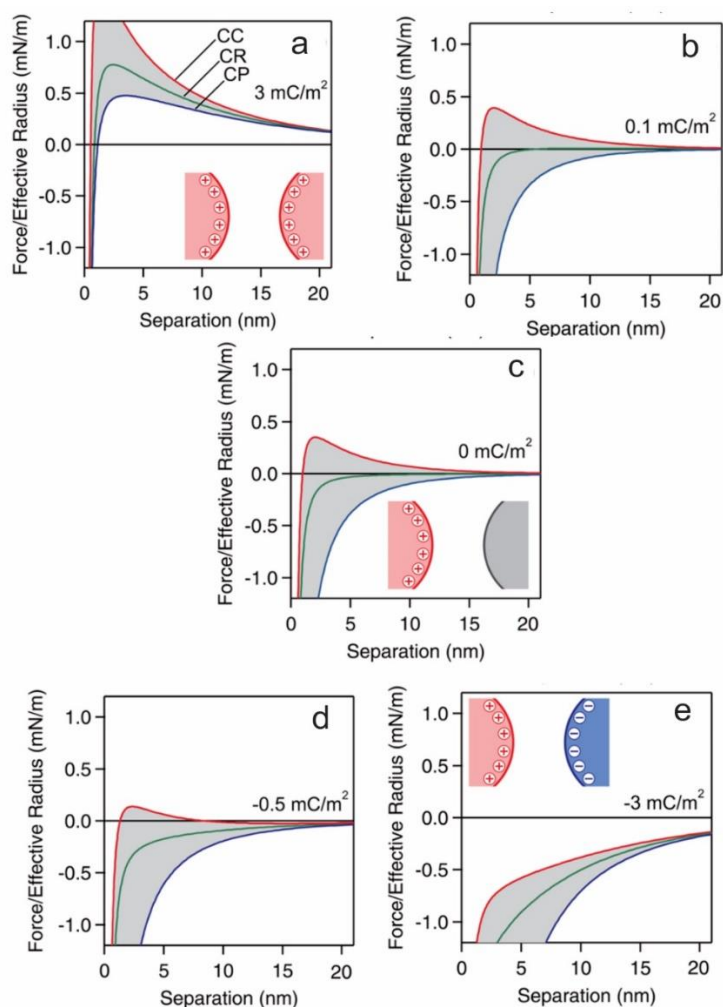


**Figure 2.10:** Interaction forces as a function of the separation distances between two charged colloidal particles. The first particle has constant charge density of  $3 \text{ mC/m}^2$  and the second particle charge density of a)  $3 \text{ mC/m}^2$  b)  $0.1 \text{ mC/m}^2$  c)  $0 \text{ mC/m}^2$  d)  $-0.5 \text{ mC/m}^2$  e)  $-3 \text{ mC/m}^2$ . (Adapted with permission from reference [38]).

while the attractive van der Waals force prevails at small separation as can be seen in figure 2.10a. In the case of an asymmetric charge density where the charge density of the second particle is reduced to  $0.1 \text{ mC/m}^2$ ,  $0 \text{ mC/m}^2$  (neutral-charged surface) and  $-3 \text{ mC/m}^2$ , the system shows more complex behavior which includes both repulsive and attractive interactions, see figures 2.10b-d [38]. Whether the interaction is repulsive or attractive is determined by the boundary conditions. The forces between oppositely charged particles with comparable charge density magnitudes are attractive, see figure 2.10e.

The above mentioned scenarios can be applied to the interactions between the STM tip and a gold coated cantilever since the STM imaging process requires the conducting tip to be biased. However, in this case the cantilever is grounded which makes our situation a neutral-charged system as in the case depicted in figure 2.10c. Therefore, a long range repulsive force on the cantilever during the approaching process of the STM tip is possible as will be illustrated and discussed in Chapter 4.

## **2.7 Adhesive theories**

Various theories can be used to explain the interactions between materials brought together such as Johnson–Kendall–Roberts (JKR) theory. In the JKR theory, when two elastic materials are brought into contact, the effect of the adhesive force within the radius of the contact must be included unlike Hertz theory [40,41, 42]. The JKR theory discusses the critical force to separate two elastic bodies (pull-off force), and estimates the adhesive pull-off force to be  $3/2\pi\gamma R$ , where  $\gamma$  is the work of adhesion

and  $R$  is the radius of the tip [43]. The theory assumes that there is a finite contact area at the pull-off force due to the adhesive force [43]. The JKR theory can be applied to large probes, soft samples and large adhesions [43,44].

Another theory which also considers the adhesive force in the interaction between two materials in contact is Derjaguin–Muller–Toporov (DMT) theory. One of the characteristics of this theory is the attraction forces act only outside the contact area, see figure 2.11 [41, 42]. The theory assumes that the contact area vanishes before the separation occurs i.e. the radius of the contact is zero [43]. In DMT theory, the adhesive pull-off force is estimated to be  $2\pi\gamma R$  which is greater than the adhesive force predicted by JKR theory [43]. To describe the contact area for small tips, high Young's moduli and low adhesion, the DMT theory is more appropriate [43, 44].

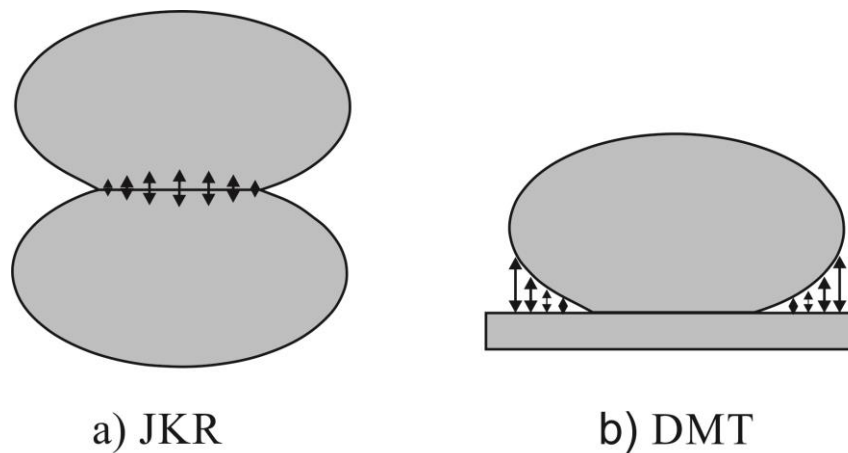


**Figure 2.11:** a) The attraction forces within the radius of the contact area are included in JKR theory. b) In DMT theory only the attraction forces outside the contact region are included.

A transition parameter called the Tabor parameter  $\mu$  can be used to determine the validity of the DMT and JKR models for any system [43]. When  $\mu < 0.1$  the DMT theory is valid, and for the case where  $\mu > 5$  the JKR theory is most appropriate [45]. The parameter  $\mu$  is given by the following [46]:

$$\mu = \left( \frac{R \gamma^2}{E^* Z_o^3} \right)^{1/3} \quad (2.14)$$

where  $R$  is the sphere's radius (for our system, the radius of the STM tip) and  $\gamma$  is the work of adhesion which was estimated to be 1.92 N/m<sup>2</sup> for our system using the following equation [46, 47]

$$\gamma = 2(\gamma_1 * \gamma_2)^{1/2} \quad (2.15)$$

where  $\gamma_1$  and  $\gamma_2$  are the surface energy of gold and Platinum (Pt) which are 1.37 and 2.691 J/m<sup>2</sup> respectively.  $Z_o$  is the interatomic spacing between atoms which is approximately equal to 0.28 nm for Au and Pt, and lastly  $E^*$  is given by [46]

$$E^* = \left( \frac{1 - \nu_1}{E_1} - \frac{1 - \nu_2}{E_2} \right)^{-1} \quad (2.16)$$

where  $E_1$  and  $E_2$  are Young's modulus for Au and Pt which are 117 and 160 GPa respectively and  $\nu_1$  and  $\nu_2$  are Poisson ratio for Au and Pt which are 0.42 and 0.39 respectively. By using the equations 2.14, 2.15, and 2.16 above,  $\mu$  for our system was found to be 1.7 which means that our experiments are in the transition region between DMT and JKR theory, and therefore neither theory can be applied to our system.

## 2.8 The relation between the cantilever deflection and Point load position

As the magnitude of the forces acting on the cantilever affects the magnitude of the cantilever deflection, the location of the applied force on the cantilever also strongly affects the cantilever deflection. The following equation shows the cantilever deflection as a function of the position of the point load on the cantilever [48]

$$\Delta x_{max} = \frac{FP^2}{6EI}(3CL - P) \quad (2.17)$$

where  $\Delta x_{max}$  is the induced end deflection,  $F$  is the force applied on the cantilever,  $P$  is the position of the point load on the cantilever,  $CL$  is the cantilever length,  $E$  is the **Young's modulus of the cantilever**, and  $I$  is the area moment of inertia. The induced deflection caused by an applied force of 10 nN at different locations on a cantilever of 350  $\mu\text{m}$  length is shown in figure 2.12.

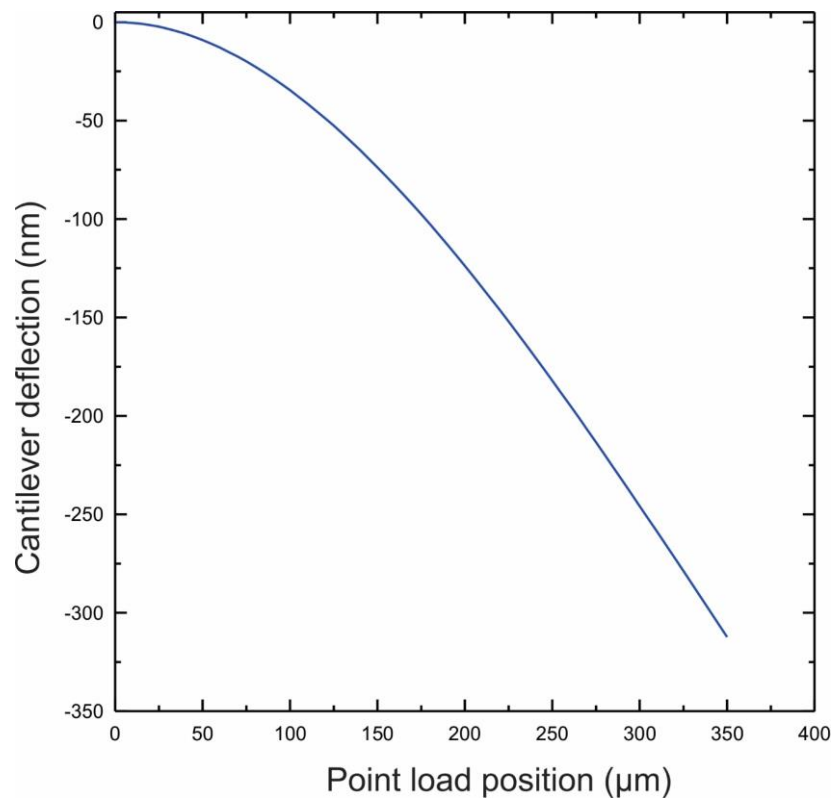


**Figure 2.12:** The cantilever deflection as a function of the point load location on the cantilever.

# Chapter 3 Experimental setup and methods

## 3.1 STM setup

In order to achieve the objective of investigating the forces acting between the tip and the surface, a new experimental setup was designed and constructed. The new set up shown in figure 3.1 consists of the following components; the STM, an optical focuser, a position sensitive detector (PSD) and a microscope connected to a charge-coupled device (CCD) camera.

The cantilever was placed into a groove of the setup platform and held by a stainless steel clip as shown in figure 3.2. In order to connect the cantilever to the STM tunneling circuit, a wire was connected to the stainless steel clip which allows the cantilever to be directly connected to the STM scanner. Great care had to be taken to ensure that neither the clip nor the cantilever was electrically connected to the base plate. After the cantilever was positioned and secured, a laser beam was focused on the free end of the cantilever. The laser focuser was placed below the platform and secured at an angle of  $70^\circ$  as shown in figure 3.1. A PSD held at an angle of  $50^\circ$  was used to record the reflected optical beam.

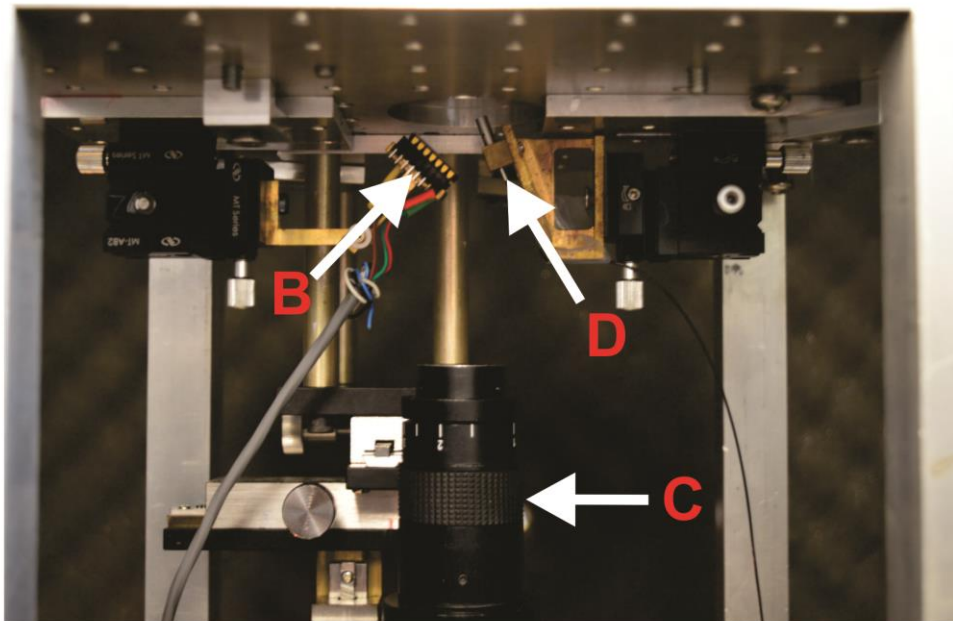
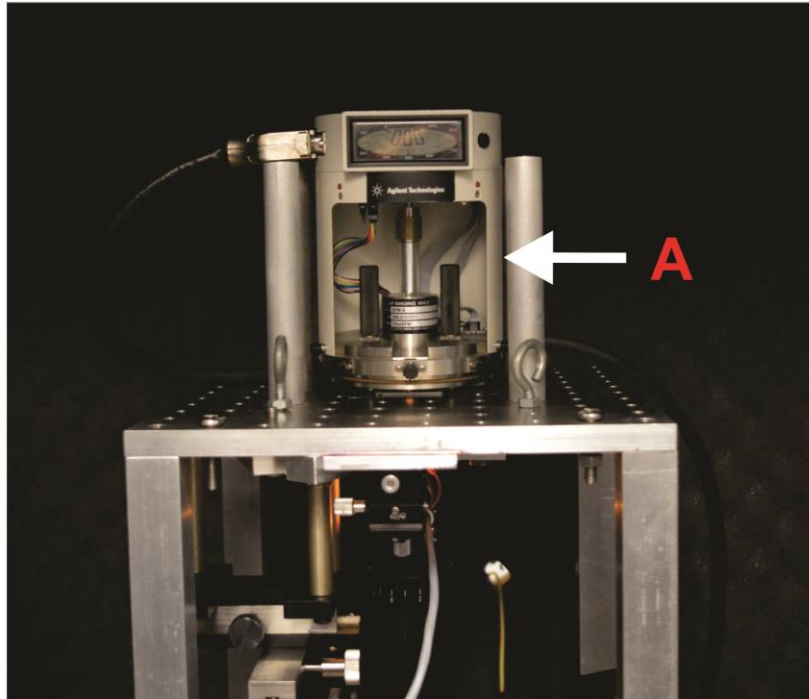


**Figure 3.1:** Photographs of the STM setup including A: the STM body, B: the PSD, C: an optical microscope connected to a CCD camera, and D: an optical focuser.

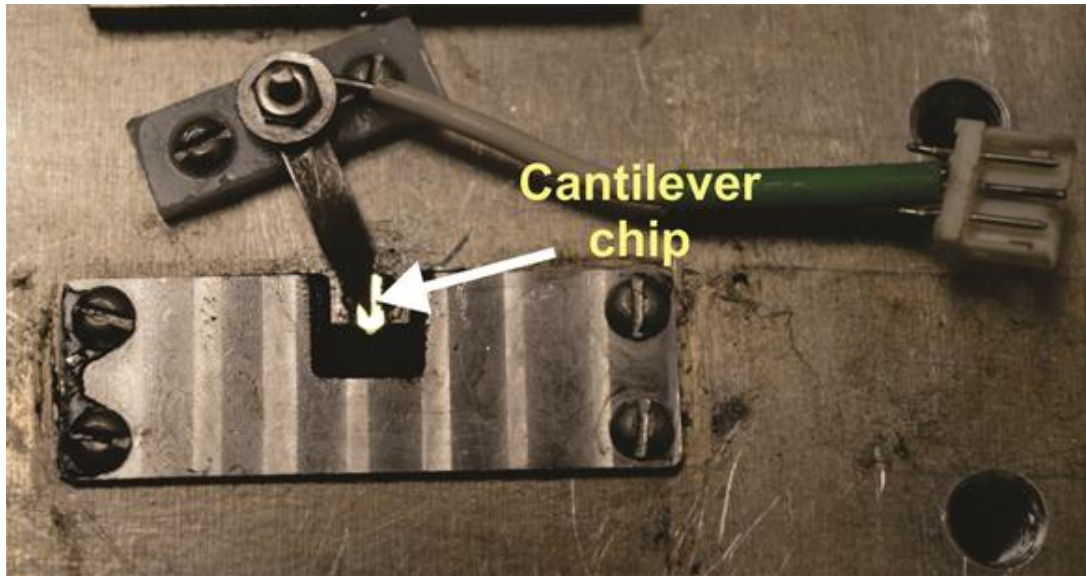


**Figure 3.2:** A photograph of the cantilever placed into a groove and held by a stainless steel clip.

In order to adjust the position of the laser beam on the cantilever and the location of the reflected beam on the active area of the PSD, both of the laser focuser and the PSD were mounted on *xyz*-translation stages.

During the experiments a PicoScan scanning probe microscope (SPM) from Agilent Technologies was used. The microscope body was mounted on the setup platform with the distance between the STM tip and the cantilever adjusted such that the tip was between 2- 4 mm from the cantilever. To close the gap between the STM tip and the cantilever, the two front screws were adjusted manually while the rear screw was turned automatically during the approach stage. The rear screw was placed on a fabricated V-shaped groove to prevent the STM from moving laterally during the approach.

In order to see and have a clear view of the position of the STM tip over the cantilever, three small mirrors angled at  $45^\circ$  with respect to the plane of the cantilever were placed around the cantilever. The front mirror and the view from below allowed us to ensure that the STM tip was directly on the cantilever as shown in figures 3.3 a and b. The location of the STM tip on the cantilever was estimated from the side view images. Finally, the position of the focused laser beam on the cantilever was also observed from below. After placing the microscope and adjusting the laser spot on the cantilever, the approach process was initiated.

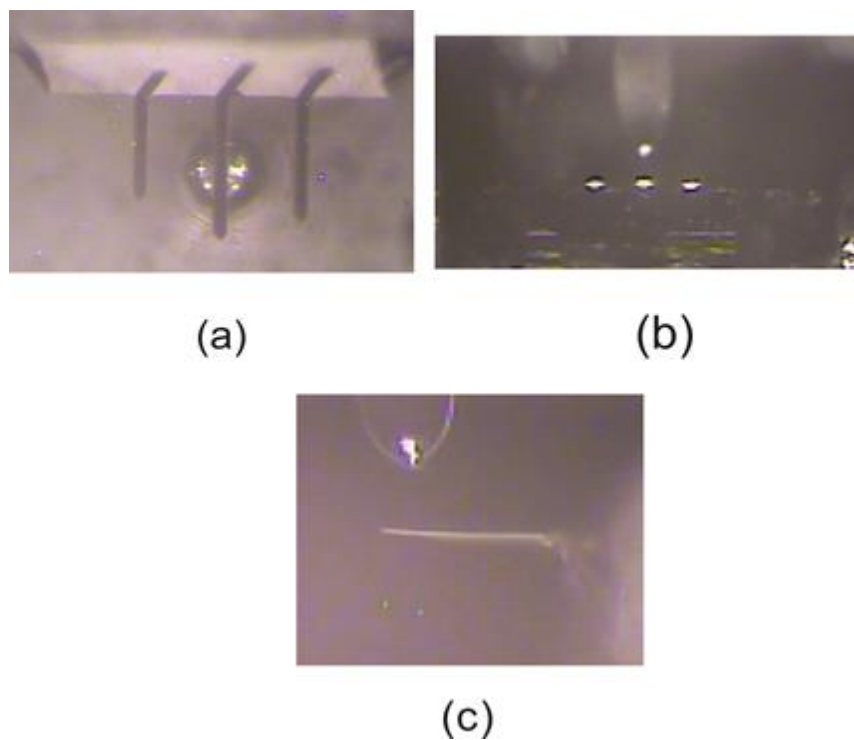


**Figure 3.3:** a) A direct view of the STM tip and the cantilever from below. b) A front view of the STM tip on the cantilever and STM tip. c) A side view of the position of the STM tip on the cantilever.

### 3.2 Laser and PSD

The laser beam used in this work was emitted by a laser diode (FMXL112-00, Clair Lasers), while the optical focuser used to focus the laser beam on the free end of the cantilever was obtained from OZ optics. To keep the intensity of the beam constant, the diode was mounted on a constant temperature stage controlled by a temperature controller. To detect the reflected beam, a PSD was used. The PSD (obtained from

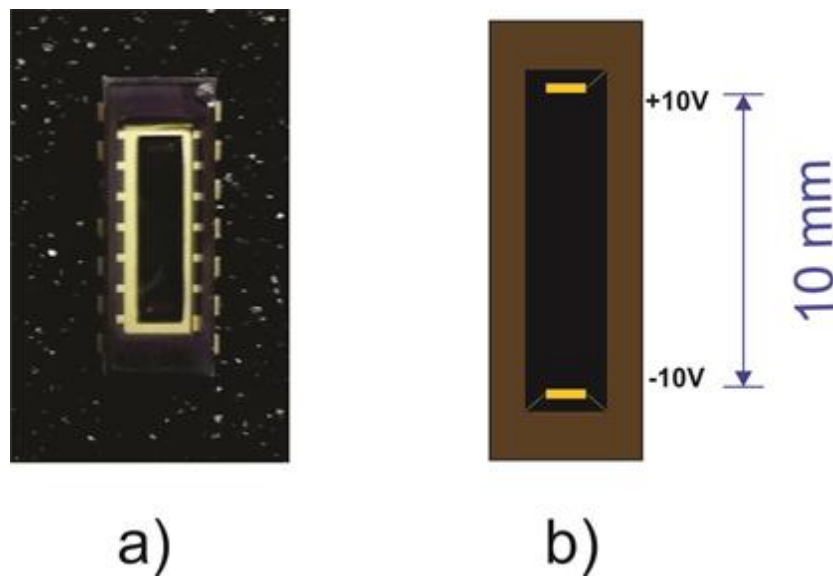


**Figure 3.4:** a) Photograph of the position sensitive detector (PSD). b) Schematic representation of the active area of the PSD.

ONTRACK) has an active area 10 mm long (figure 3.4). The output of the PSD is proportional to the beam position on the PSD surface. When the laser beam hits the active area of the PSD, it generates a photoelectric current that is proportional to the location of the incident beam on the active area of the PSD. The current is then converted to a voltage that is read and recorded by a computer.

## **3.3 Methodology**

### **3.3.1 Sample preparation**

The microcantilevers used in this work, obtained from MikroMasch (CSC38), were on the order of  $350 \pm 5 \mu\text{m}$  long,  $33 \pm 3 \mu\text{m}$  wide and  $1.0 \pm 0.5 \mu\text{m}$  thick. Using sputter deposition, a 5 nm film of inconel (0.8Ni + 0.2Cr) was deposited on the cantilever to act as an adhesive layer. The inconel deposition was conducted at a sputtering power of 40 W and deposition rate of  $0.2 \text{ \AA/s}$ . Without breaking the vacuum, a 40 nm gold film was then deposited at a deposition rate of  $0.2 \text{ \AA/s}$  and power of 10W for  $33 \pm 1$  minutes.

Prior to use, the cantilevers were cleaned with a Piranha solution ( $\text{H}_2\text{SO}_4:\text{H}_2\text{O}_2 = 3:1$ ) to eliminate organic contaminants on the gold-coated cantilevers. The cantilevers were immersed in a Piranha solution for 10 minutes and then rinsed in ethanol and water two times. Subsequently, the cantilevers were dried in the oven at  $270 \text{ }^\circ\text{C}$  for 2 hours to minimize the size of the water layer on the surface of the cantilevers.

### **3.3.2 SEM of STM Tips**

In this work, electrochemically etched  $\text{Pt}_{0.8}\text{Ir}_{0.2}$  tips were used as obtained from Keysight Technologies (N9801A). Scanning Electron Microscopy (SEM) was used to provide precise measurements of the dimensions of each tip. SEM images were processed in CorelDraw software in order to measure the tip radius  $r$ , the cone half angle  $\theta$ , and the height of cone  $h$  (see figure 3.5). A precise measurement of these

quantities was of fundamental importance for the accurate determination of the tip to surface separation and the total force. Similar to the cantilevers, the STM tips were cleaned by Piranha solution and dried in the oven before use.

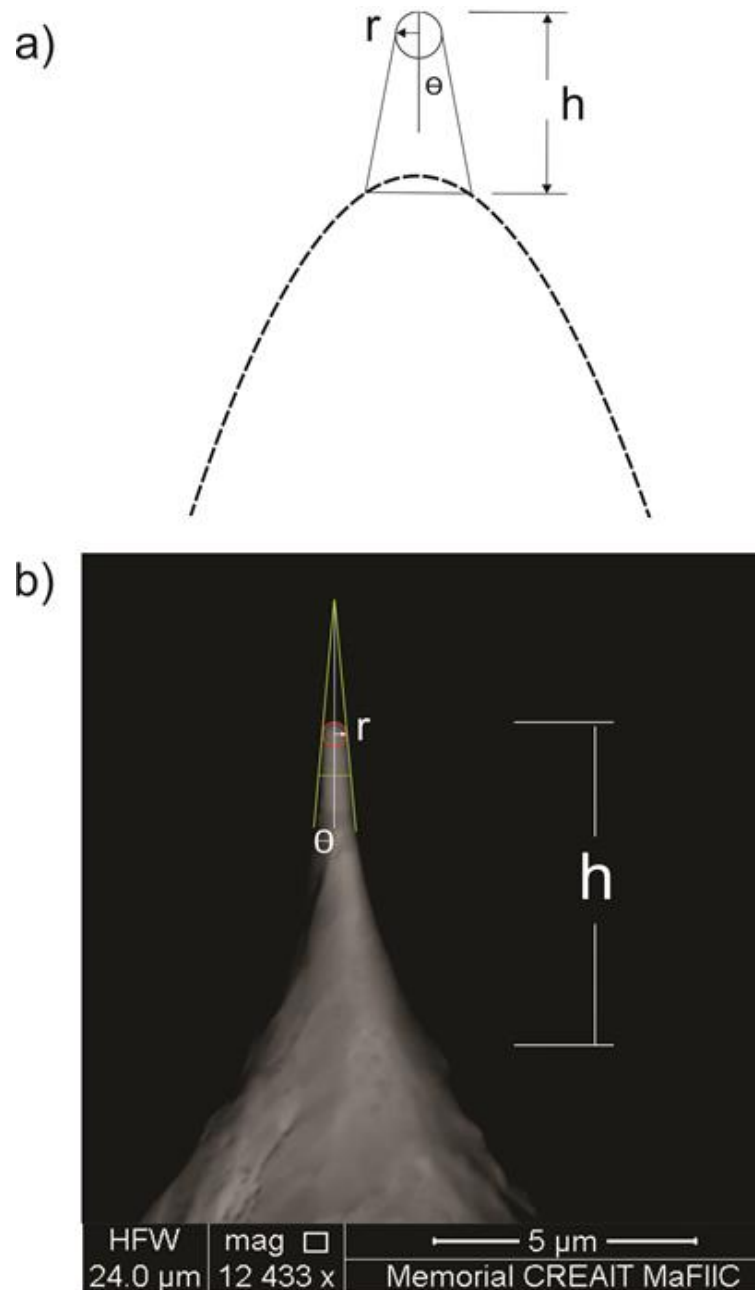


**Figure 3.5:** a) Schematic representation of the modeled STM tip. b) SEM image of the STM tips used in this work.

### 3.3.3 Calibration of the Optical Beam Deflection System (OBDS)

An optical beam deflection system was used in this work to monitor the deflection of the cantilever. Knowledge of the parameters of the OBDS was crucial for obtaining precise measurements since it affects the voltage measured by the PSD. The distance  $L$  (see figure 3.6) was measured by using a method developed by Xu et al [49]. In order to accomplish this, the PSD and the laser focuser were secured at angles of  $\phi$  and  $\theta_1$  respectively. The measured signal of the reflected beam on the PSD was recorded as  $h_1$ . The laser focuser was then rotated to angle  $\theta_2$ . The spot of the reflected beam on the PSD changed to  $h_2$ . The distance between the Cantilever and the PSD was determined by

$$\Delta h = L_0 \times \frac{\sin(\theta_2 - \theta_1)}{\sin(\theta_2 - \beta + \phi)} \quad (3.1)$$

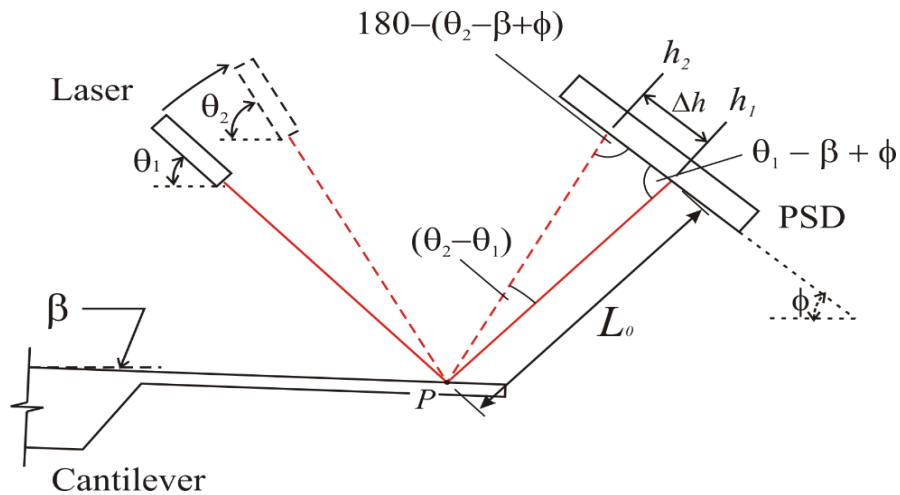


**Figure 3.6:** Schematic representation indicating how to measure the distance between the cantilever and the PSD. (adapted with permission from Reference 49).

where  $\Delta h$  is the change in position of the reflected beam on the PSD surface, and  $\beta$  is the angle of inclination of the cantilever which for us was zero.

The PSD signal was related to the cantilever deflection by using a program based on the mathematical model developed in [50]. To obtain the actual cantilever deflection, geometric optics and vector analysis were used by the authors. As illustrated in figure 3.7, the system was defined by geometrical variables such as the angle of the laser beam  $\theta$ , the PSD angle  $\zeta$ , the cantilever length  $CL$ , the initial cantilever-PSD separation  $L_0$ , and the position of the laser on the cantilever  $D$ .

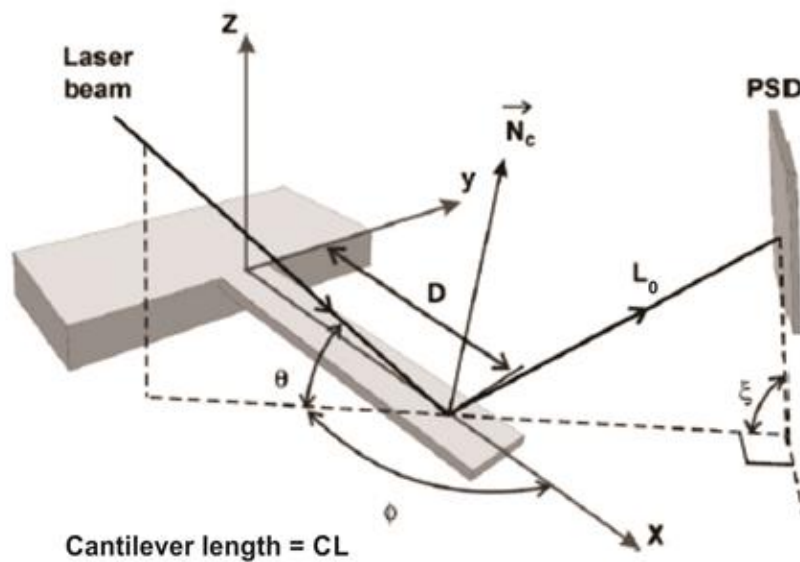


**Figure 3.7:** Schematic representation of the laser beam deflection system analysis.

[Adapted with permission from Reference 50]

The positions of the laser beam and the STM tip on the cantilever were determined by processing images taken by the CCD camera using CorelDraw software (see figure 3.8). The relationship between the PSD signal and the cantilever deflection is shown in figure 3.9.

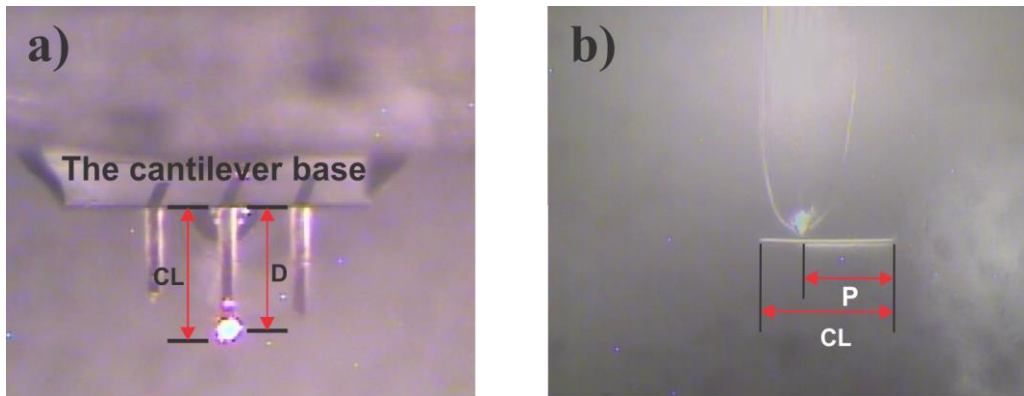


**Figure 3.8:** a) A direct view of the position of the laser beam on the cantilever. b) A side view of the position of the STM tip on the cantilever. These images were used to obtain CL, P and D.

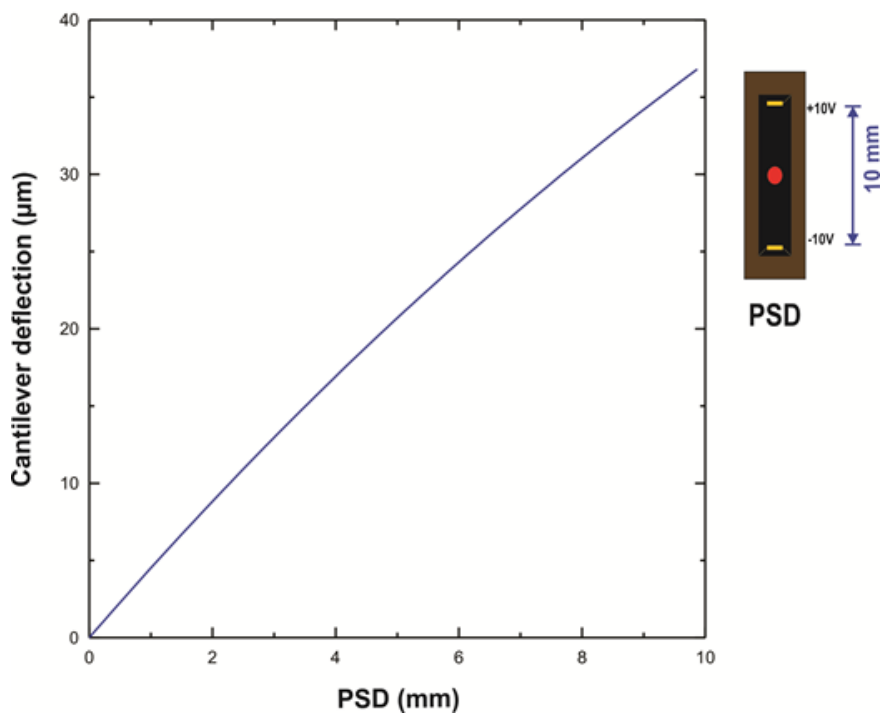


**Figure 3.9:** The relationship between the position of the optical beam on the PSD and the microcantilever deflection.

In order to determine the magnitude of the force generated by the cantilever deflection, the value of the deflection was substituted in the point load beam deflection equation [48]:

$$F = \Delta x_{max} \frac{6EI}{(3CL - P)P^2} \quad (3.2)$$

where  $\Delta x_{max}$  is the induced end deflection,  $P$  is the position of the point load on the cantilever,  $CL$  is the cantilever length,  $E$  is the Young's modulus of the cantilever, and  $I$  is the area moment of inertia. This force is the value of the total force due to the interactions between the STM tip and the cantilever surface including the van der Waals force, the capillary force and the repulsive force.

### 3.4 Spring constant calibration

The spring constant of the cantilevers used in this work ranged from 0.003 - 0.13 N/m. Knowledge of the exact spring constant of each cantilever is important for comparing the experimental conditions under which cantilevers were used. Therefore, the resonant frequency of each cantilever was measured using the cantilever tuning feature in our AFM system. Then, the spring constant ( $k$ ) was calculated by substituting the measured value of the resonant frequency ( $\nu_0$ ) in the following equation [51]

$$k = 2\pi^3 CL^3 w \sqrt{\rho/E} (\nu_0)^3 \quad (3.3)$$

where  $CL$  and  $w$  are the length and the width of the cantilever, respectively,  $E$  is Young's modulus, and  $\rho$  is the density of the silicon.

# Chapter 4 Results and Discussion

In this chapter, we will discuss the experimental results obtained while attempting to measure the forces between an STM tip and a Au-coated cantilever. In section 4.1, the experimental procedures that were followed to investigate the STM tip-cantilever interactions are presented. Detailed discussions regarding the obtained experimental results are presented in section 4.2.

## 4.1 Experimental procedure

The cantilever was initially placed in the setup, described in section 3.1, and the microscope was mounted on the setup stage. The optical beam was then focused on the free end of the cantilever and the reflected beam was detected and its position recorded using a PSD (see figure 4.1). The position of the reflected beam was first recorded for 180 seconds to obtain a baseline used to determine the initial position of the cantilever. The approach was started as the STM tip was lowered towards the cantilever at a constant speed  $v$  by the use of a computer controlled screw at the rear of the STM head. During this stage the piezo actuator in the STM scanner oscillated with an angular frequency ( $\omega$ ) up and down until the set tunneling current of 0.1 nA.

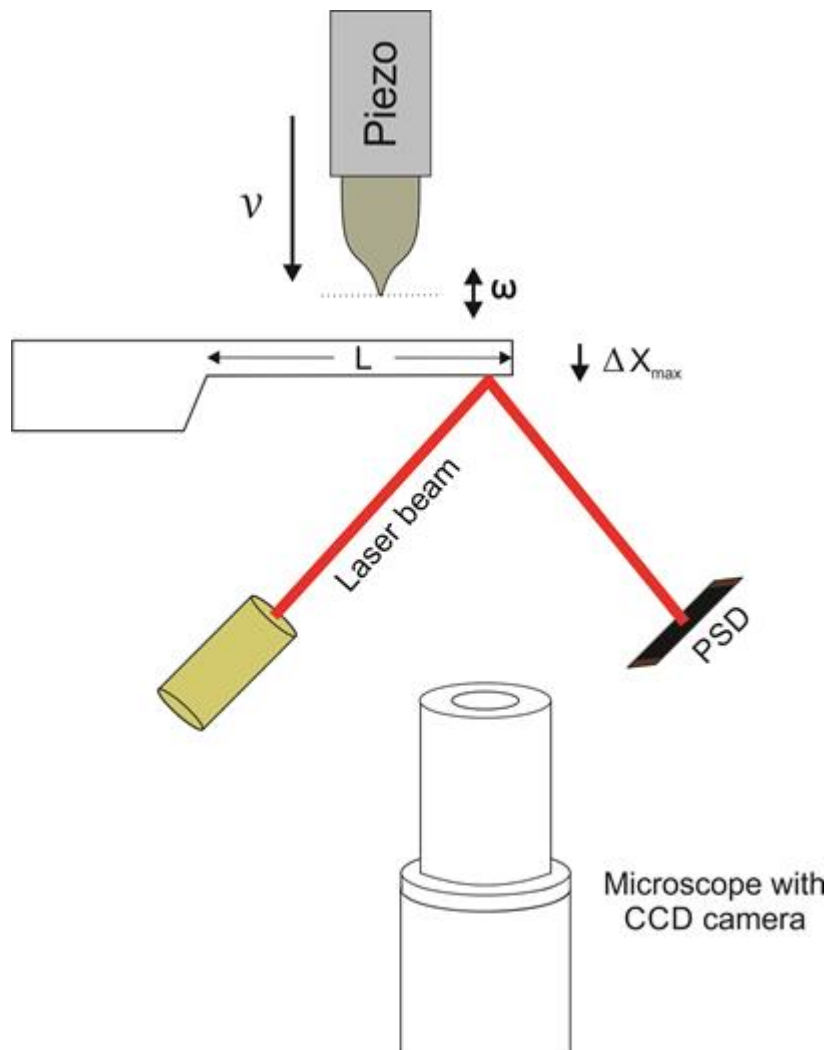


**Figure 4.1:** Schematic representation showing the configuration of the major components of the experimental setup.

was reached. For the tunnelling current of 0.1 nA, the separation between the STM tip and the cantilever surface can be estimated by substituting the value of the current and the cross-sectional area of the tip into equation 2.5. After the set current was reached, data was recorded for approximately 20 seconds before the withdraw process was initiated. During the withdraw process the piezoelectric tube in the scanner was fully

retracted to lift the tip away from the cantilever surface and the rear screw was actuated to lift the STM head up and away from the cantilever.

## **4.2 Results and discussion**

Although many experiments were conducted, we report here on five results showing typical behaviour of the system. Conducting these experiments was very difficult because of the need to position a 250  $\mu\text{m}$  diameter tip on a cantilever only 50  $\mu\text{m}$  wide. In addition, the STM tip had a tendency of coming off the cantilever during the approach which ruined the experimental results and sometimes the tip itself.

### **4.2.1 First Experiment**

The response of the cantilever to the change in current and the piezo movement collected as the tip was approaching, engaged, and withdrawing is shown in figure 4.2. To highlight the important features of the data, the horizontal time axis was broken for the periods of 20 to 175 sec and 190 to 280 sec. The vertical axis was also divided into two major portions. The upper section shows the current in units of nA while the lower portion shows the cantilever deflection and piezo movement in arbitrary units. As stated previously, the approach was started at  $t = 180$  sec (point A) at which point the piezo started to oscillate (as shown by the green data) in an attempt

to reach the tunnelling current set point<sup>6</sup>. As the STM tip came closer to the cantilever, the attractive forces between the cantilever and the STM tip increased but

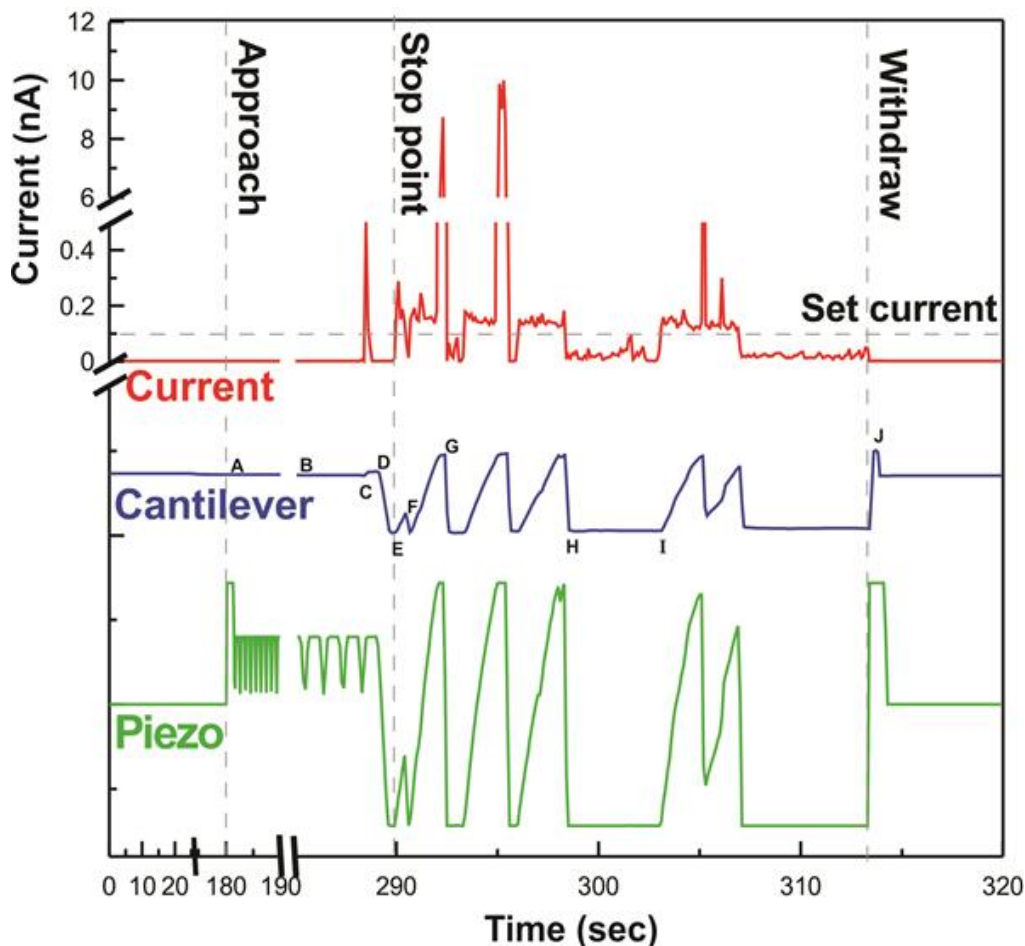


**Figure 4.2:** The changes in the tunneling current (red), PSD signal (blue) and the piezo motion (green) as a function of time when the tip was approaching, engaged and withdrawing from the Au-coated cantilever surface.

were still not sufficiently strong enough to make the cantilever deflect upward (point **B** in figure 4.2). As the tip continued approaching to reach the tunnelling current set point, the cantilever deflected downward as seen at point **C** in figure 4.2. This deflection can be seen more clearly in figure 4.3.

<sup>6</sup> The oscillation of the STM tip during the approach is a built-in feature of our STM system.

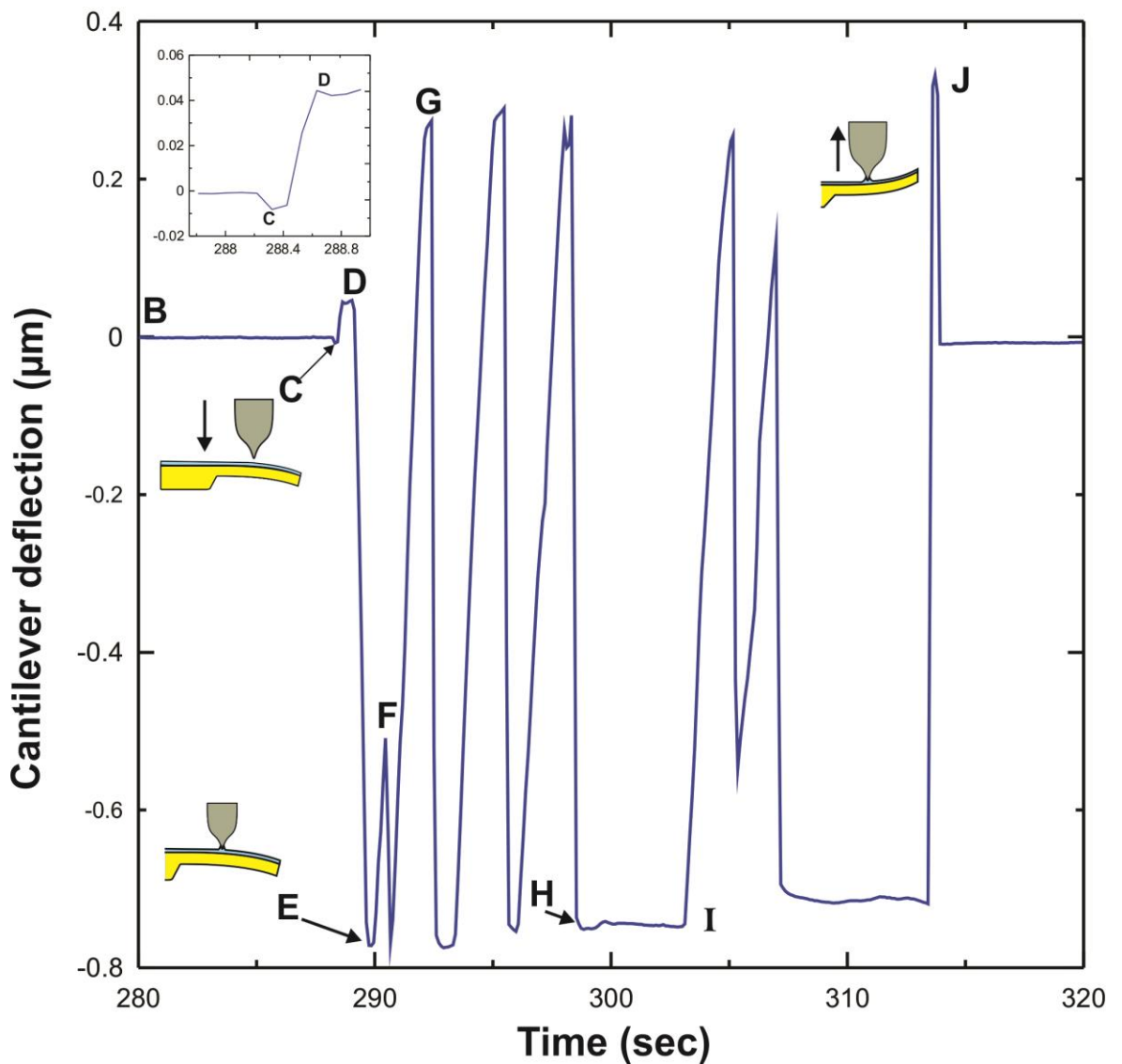


**Figure 4.3:** The cantilever deflection as a function of time in response to the STM tip. The insert is a magnified portion of the cantilever deflection showing points C and D.

It is possible that this deflection results from long range DLVO interactions. As it was noted in section 2.6, a repulsive force can act on the cantilever from the interaction between a charged STM tip and a grounded cantilever at large separation [40]. When the tip came close to the water layer surface, the attractive forces, mainly capillary

force, caused the cantilever to jump into contact<sup>7</sup> with the tip (point **D**) [52]. Further approaching caused the tip-cantilever separation to decrease and reach a point where the repulsive forces started to dominate. As a result, the cantilever deflected downward (points **D** to **E**). As the set tunnelling current was reached, the approaching process was stopped, as indicated by point **E** in figure 4.2. At point **E**, the tunnelling current (as shown by the red data) was slightly larger than the tunnelling current set point, and as a result the piezoelectric tube in the scanner retracted and the cantilever deflected upward. Based on equation 2.5, the tip-sample separation distance at point **E** was estimated to be 7 Å. The deflection at point **F** was caused by the retraction of the piezo to maintain the tunnelling current set point. When the piezo retracted, the tip-cantilever separation distance increased. The repulsive force acting between the tip and the cantilever decreased since the magnitude of the force is strongly affected by the separation. The upward deflection of the cantilever seen at point **G** in figure 4.2 is believed to be caused by the formation of a water bridge between the STM tip and the cantilever. Despite the piezo being fully retracted to increase the separation distance between the STM tip and the cantilever surface to maintain the current set point, the presence of the water layer caused the cantilever to remain in contact with the STM tip.

It is interesting to note that as the piezo elongated to its maximum, which caused the cantilever to deflect downward (between points **H** and **I**), the tunnelling current went to zero. This elongation caused the position of the tip on the cantilever to shift by 0.3 pm in a direction parallel to the length of the cantilever, however, it is not believed

---

<sup>7</sup> By contact means that the STM tip is only a few angstroms away from the cantilever. We use the term *physical contact* when the cantilever is touching the cantilever causing the tunneling current to go to infinity.

that this change in the position of the tip affected the tunnelling current. A definitive explanation of this phenomenon has not yet been obtained.

The deflection at point **D** was found to be  $46 \pm 10$  nm. The large uncertainty observed in the cantilever deflection is a result of the uncertainties in the PSD signal, the laser angle, the position of the point load, the position of the laser spot on the cantilever, and the length of the cantilever. Using equation 3.2 the point load force which acted on the cantilever at  $P = 260 \pm 5$   $\mu\text{m}$  from the base was found to be  $2.4 \pm 0.5$  nN. This force is the magnitude of the total force due to the interactions between the STM tip and the cantilever surface including the van der Waals and the capillary force.

To compare the experimentally measured force to the van der Waals force, the characteristics of the tip used in the experiment and the distance between the STM tip and the cantilever were substituted into equation 2.6 (see Chapter 2). The STM tip used in this experiment had a radius of  $216 \pm 14$  nm, cone half angle of  $7.1 \pm 0.5$  degree and cone height of  $5.3 \pm 0.4$   $\mu\text{m}$ . The experiment was conducted at a relative humidity of 24 %, and under such conditions a water layer of  $5 \pm 1$  nm thick was present on the cantilever surface [53]. By substituting the value of the tip-cantilever separation, which is approximately equal to the water layer thickness, into equation 2.6, the van der Waals force was found to be  $0.16 \pm 0.04$  nN. The magnitude of the capillary force was estimated by substituting the value of the relative humidity, the thickness of the water layer (5nm) and the time during which the cantilever started to deflect upward until the attractive forces reached the maximum ( $0.20 \pm 0.05$  s) into equation 2.13 giving a capillary force of  $2.2 \pm 0.4$  nN. Therefore, theoretically, the

total attractive force between the STM tip and the cantilever was  $2.4 \pm 0.4$  nN, which is excellent agreement with the experimentally measured force of  $2.4 \pm 0.5$  nN.

When the separation distance between the tip and the cantilever was decreased, the repulsive forces started to appear and dominate causing the cantilever to deflect downward (**D-E** figure 4.3). Based on the current reading at point **E**, the separation distance between the STM tip and the cantilever was found to be 7 Å. Because the net force acting on the cantilever at point **E** should equal to zero, the sum of the van der Waals, capillary, cantilever force and the repulsive force at point **E** was zero. The van der Waals force at 7 Å was found to be  $8.2 \pm 0.5$  nN. The capillary force was estimated by substituting the separation distance (7 Å) and the water height on the tip (4.3 nm) into equation 2.12. The capillary force was thus found to be  $28 \pm 2$  nN. From the deflection at point **E** the force was found to be approximately  $45 \pm 6$  nN. The repulsive force that was acting on the cantilever when the tip was 7 Å far from the cantilever was equivalent to the sum of all the van der Waals, capillary and the cantilever force, and was found to be  $81 \pm 9$  nN.

In the withdrawal process, the STM tip was retracted from the cantilever. The water bridge caused the cantilever to adhere to the tip (point **J** in figure 4.3) until the pull-off force of the tip overcame the adhesive force. The pull-off force was estimated to be  $18 \pm 4$  nN. The contact time allowed a thick water bridge to build between the STM tip and the cantilever making the adhesion force larger than the total attractive forces at point **D** [54]. During the withdrawal process, the adhesion force of the meniscus acted against the pull-off.

The instability of the cantilever during the experiment between points **D** and **J** shows that imaging the cantilever using STM would not be easily achieved as previously reported by Lacy et al [8]. This is because during imaging the piezo moves the STM tip in 3 directions which would make a noticeable change in the forces acting on the cantilever.

### 4.2.2 Second Experiment

An additional experiment was conducted under the same conditions as the previous experiment except that the STM tip was located at  $280 \pm 5 \mu\text{m}$  from the base of the cantilever. Figure 4.4 shows the cantilever deflection, the movement of the piezo scanner and the change in the tunneling current during the experiment. The approaching process was initiated at  $t = 180 \text{ s}$  as seen at point **A** in figure 4.4. When the STM tip came close to the surface of the water layer, the cantilever deflected downward at point **B**. The same deflection was observed in the previous experiment which is speculated to be caused by the interactions between the charged tip and grounded cantilever at large separation [40]. As the STM tip continued approaching, the attractive forces became stronger which caused the cantilever to deflect upward and snap into contact with the tip (see point **C** in figure 4.5). The cantilever deflection at point **C** was found to be  $62 \pm 10 \text{ nm}$ . Substituting the magnitude of the cantilever deflection ( $62 \pm 10 \text{ nm}$ ) in equation 3.2, the total attractive forces acting on the cantilever at  $P = 280 \pm 5 \mu\text{m}$  from the base was found to be  $2.8 \pm 0.4 \text{ nN}$  which was similar to the attractive force in the first experiment.

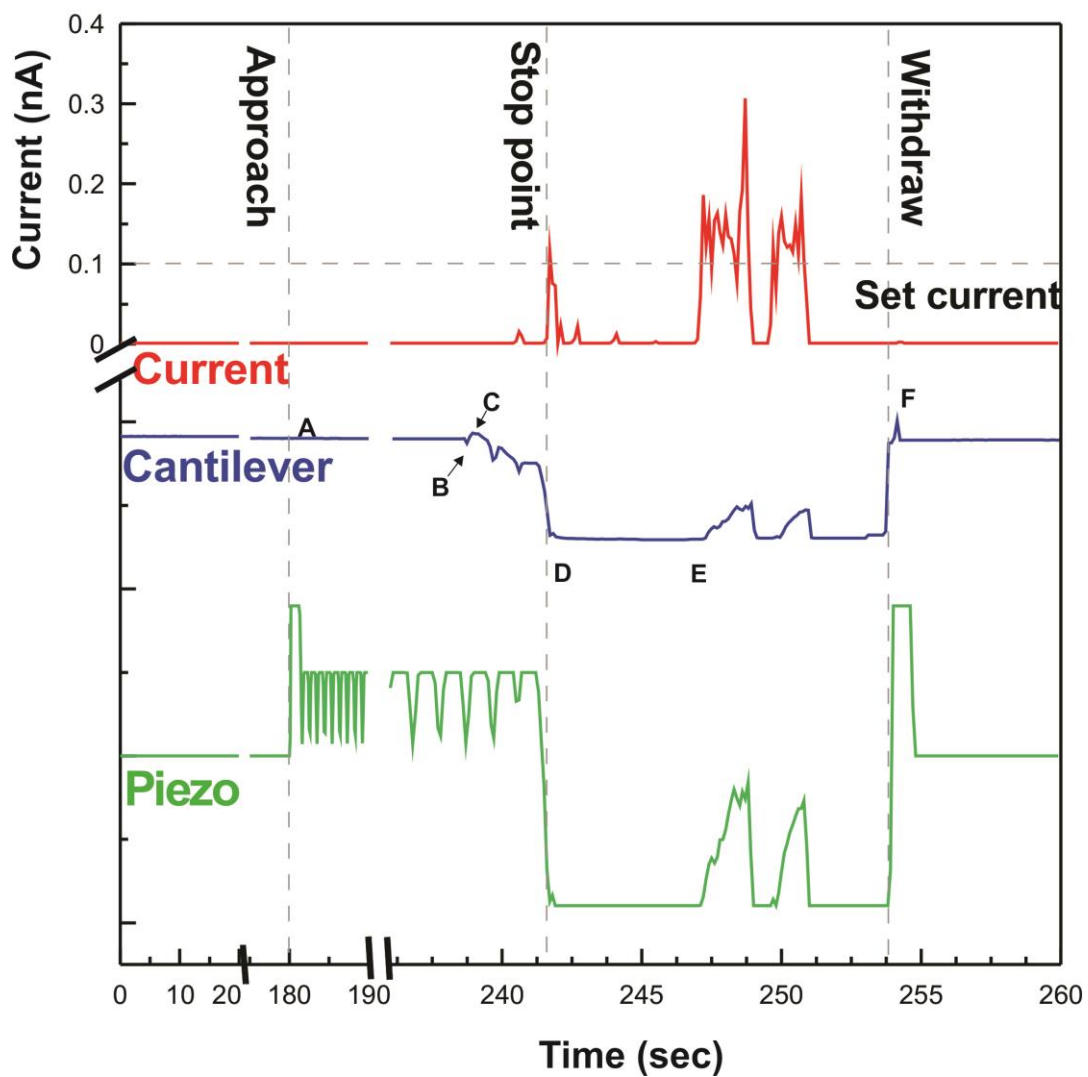


**Figure 4.4:** The changes in the tunneling current (red), PSD signal (blue) and the piezo motion (green) as a function of time when the tip was approaching, engaged and withdrawing from the Au-coated cantilever surface.

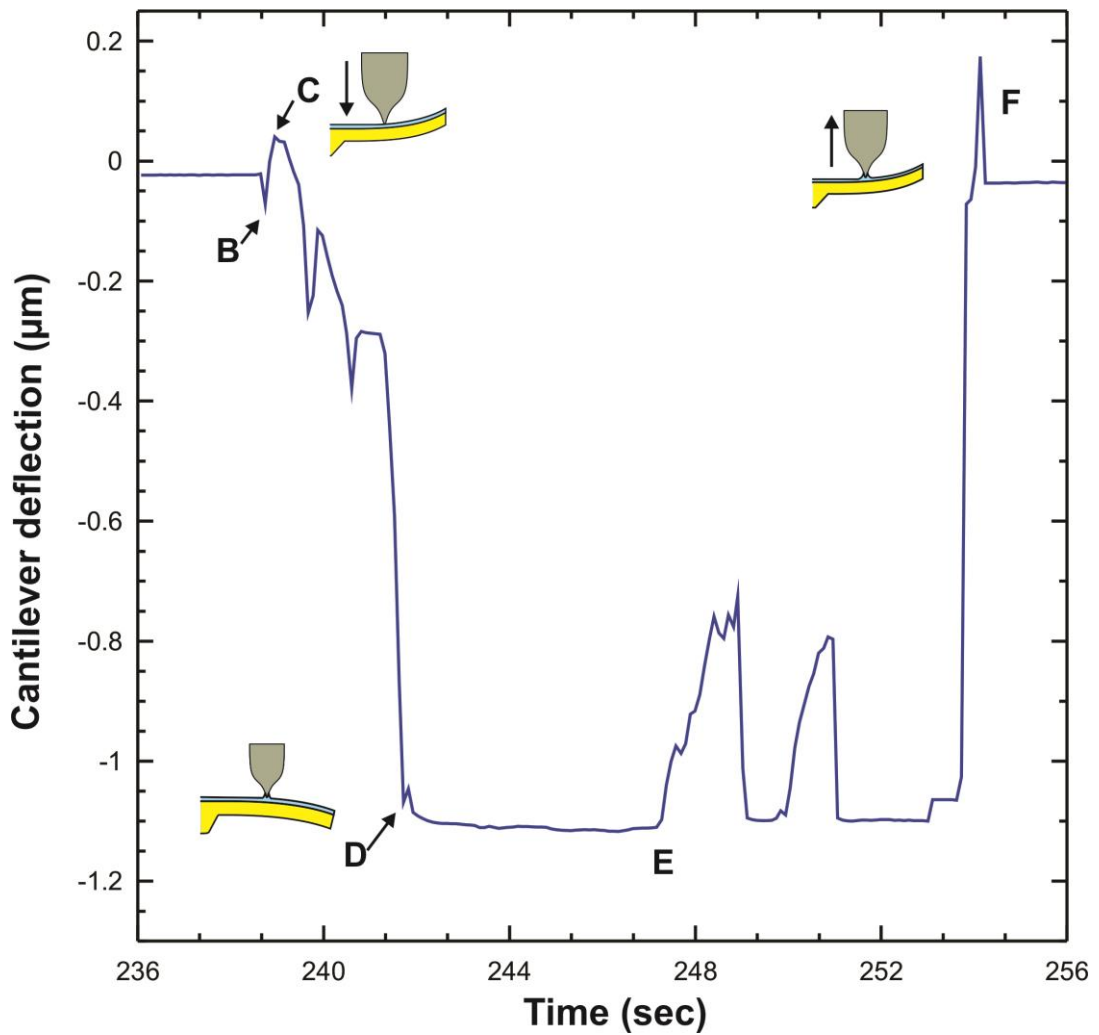


**Figure 4.5:** The cantilever deflection as a function of time in response to the STM tip.

As stated previously, the conditions of this experiment were similar to the previous experiment except that the location of the STM tip on the cantilever was different.

The calculated van der Waals force acting on the cantilever at point **C** was equal to the magnitude of the calculated van der Waals force in the previous experiment ( $0.16 \pm 0.04$  nN). By substituting the time during which the cantilever started to deflect upward until the attractive forces reached the maximum ( $0.24 \pm 0.05$  s) into equation 2.13, the magnitude of the capillary force acting on the cantilever at point **C** was found to be  $2.2 \pm 0.2$  nN which was also equivalent to the capillary force magnitude

in the previous experiment. Therefore, the total calculated attractive force acting on the cantilever was  $2.4 \pm 0.2$  nN. The experimentally measured force was larger than the theoretically calculated forces and the magnitude of the measured force in the previous experiment by 0.4 nN. Since only the location of the STM tip on the cantilever in this experiment was not the same as in the first experiment, the difference in the measured force can be attributed to the change in the STM location. The thickness of the water layer where the STM tip was located in this experiment was not the same as the previous one which influenced the magnitudes of the calculated van der Waals force and the capillary force at point **C**.

At point **C**, the STM tip continued approaching toward the cantilever in order to reach the set tunnelling current, and thus the repulsive forces started to dominate and the cantilever started to deflect downward (points **C** to **D**). At the moment the set tunneling current was reached the approach process was stopped as indicated by point **D** in figure 4.4. The sum of the van der Waals, capillary, cantilever force and the repulsive force should be zero since the cantilever was at equilibrium at point **D**. From the deflection at point **D**, the cantilever force was found to be approximately  $50 \pm 8$  nN. Based on the separation distance between the STM tip and the cantilever at point **D**, the van der Waals and the capillary force were found to be  $8.2 \pm 0.5$  nN and  $28 \pm 2$  nN respectively. Therefore, the repulsive force was acting on the cantilever at point **D** was found to be  $86 \pm 11$  nN. The repulsive force in this experiment was larger than the repulsive force in the previous experiment, but within the experimental uncertainties. The difference in the repulsive forces (4 nN) can be a result of the accuracy of the water layer thickness determination at the point where the STM tip was located on the cantilever. Between points **D** and **E**, even though the piezo was

fully elongated, the tunnelling current went to zero as was observed in the first experiment.

When the withdraw process was initiated at point **F**, the cantilever was adhered to the STM tip until the pull-off forces overcame the adhesive forces. The deflection of the cantilever at point **F** shows that a pull-off force of  $13 \pm 4$  nN was acting against the adhesive forces. The contact time between the STM tip and the cantilever allowed a thicker water bridge to build between the STM tip and the cantilever, and thus the adhesive forces acting on the cantilever were larger than the attractive forces at point **C**.

As can be observed, the location of the STM tip affected the deflection of the cantilever. Even though the experiment shows that the attractive forces was only 0.4 nN larger than the previous experiment, the cantilever deflection was 24 nm larger than the previous experiment. In addition, in this experiment the deflection of the cantilever as a result of the repulsive forces was  $1.1 \pm 0.2$   $\mu\text{m}$  while in the previous experiment the cantilever deflection was  $0.8 \pm 0.1$   $\mu\text{m}$ . The large difference in the deflection is attributed to the location of the point load on the cantilever which affected the response of the cantilever.

### **4.2.3 Third Experiment**

A subsequent experiment was conducted under a relative humidity of 27% with a different cantilever with a spring constant of  $0.021 \pm 0.001$  N/m. The STM tip was located at  $308 \pm 5$   $\mu\text{m}$  from the base of the cantilever. As in the previous experiments,

the data was collected for 180 seconds before the approaching process was initiated as seen at point **A** in figure 4.6. When the STM tip came in contact with the water layer at point **C**, the cantilever deflected upward and then snapped into contact with the tip at point **D**. A magnified portion of the cantilever deflection in units of  $\mu\text{m}$  is shown in figure 4.7. As the cantilever jumped into contact with the tip at point **D**, the feedback circuit sensed that the set point current was reached and the piezo stopped oscillating between points **D** and **E**. The current between points **D** and **E** was higher than the set current, but was not maximized. The cantilever was continuing to deflect toward the STM tip and the current was increasing correspondingly (**D-E** in figure 4.6). Following this, the cantilever jumped into physical contact with the tip between points **E** and **F**. At point **F**, the piezo was fully retracted in an attempt to pull the tip away from the cantilever to decrease the current, but the cantilever was adhered to the tip. The change in the deflection of the cantilever and the current from point **C** to point **F** happened in approximately 1-2 seconds. The current reached a maximum (10 nA) because the piezo was not fast enough to response to the feedback loop. At a relative humidity of 27% the height of the water layer on the cantilever was calculated to be  $7 \pm 2$  nm [53]. **From the first “snap-in” deflection, the strength of the attractive forces was found to be  $27 \pm 2$  nN.** Based on the current at point **D**, the separation distance between the tip and the cantilever was approximated to be  $6 \text{ \AA}$ . By using equation 2.5, the van der Waals force at  $6 \text{ \AA}$  was calculated to be  $11.2 \pm 0.8$  nN. The magnitude of the capillary force was estimated by using equation 2.12 and was found to be  $17 \pm 3$  nN. Therefore, theoretically, the total attractive force between the STM tip and the cantilever was  $29 \pm 4$  nN, which is larger than the experimentally measured force ( $27 \pm 2$  nN) but within the experimental error.

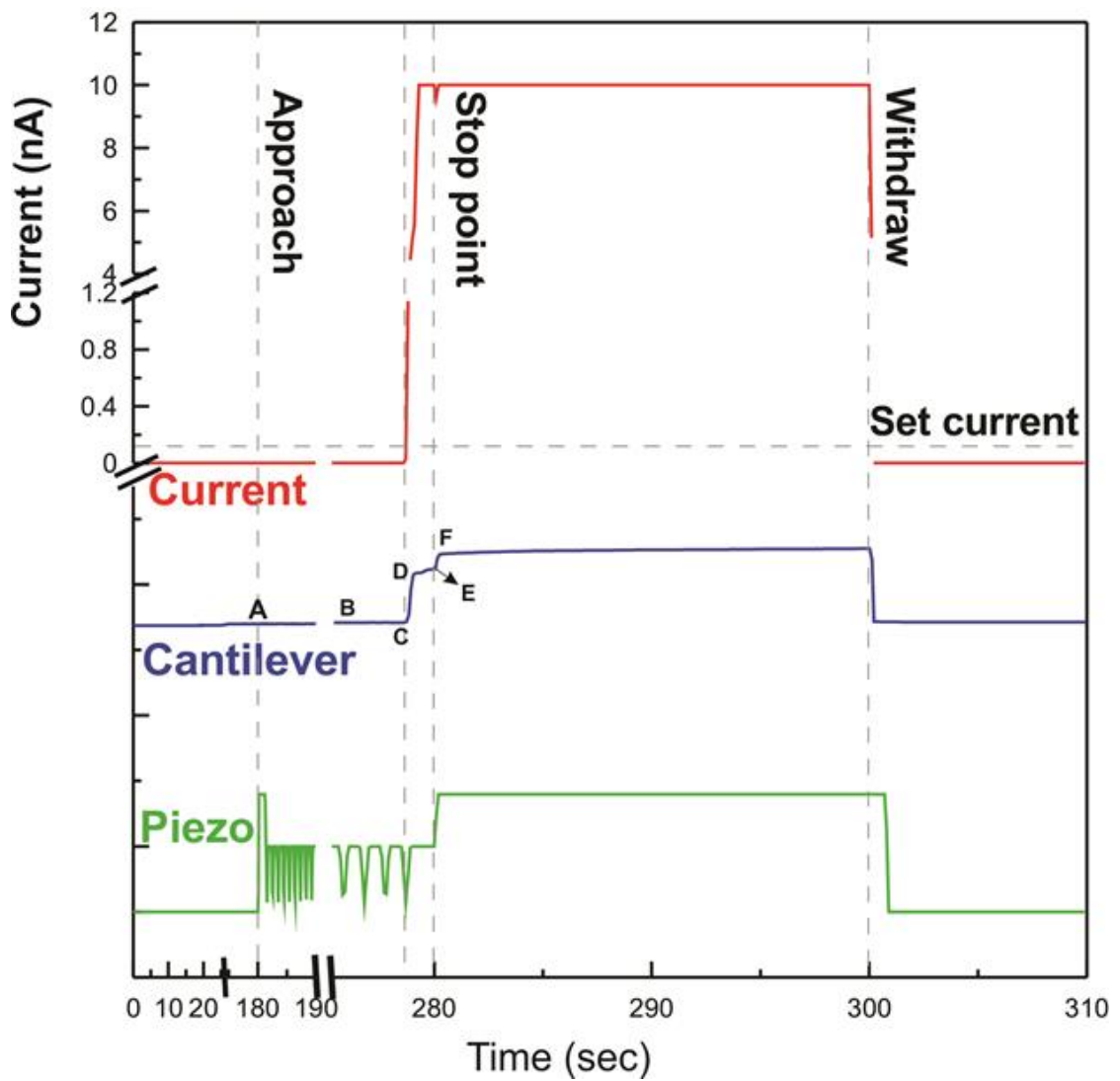


**Figure 4.6:** The changes in the tunneling current (red), PSD signal (blue) and Piezo motion (green) in response to the approach and withdrawal of the STM tip.

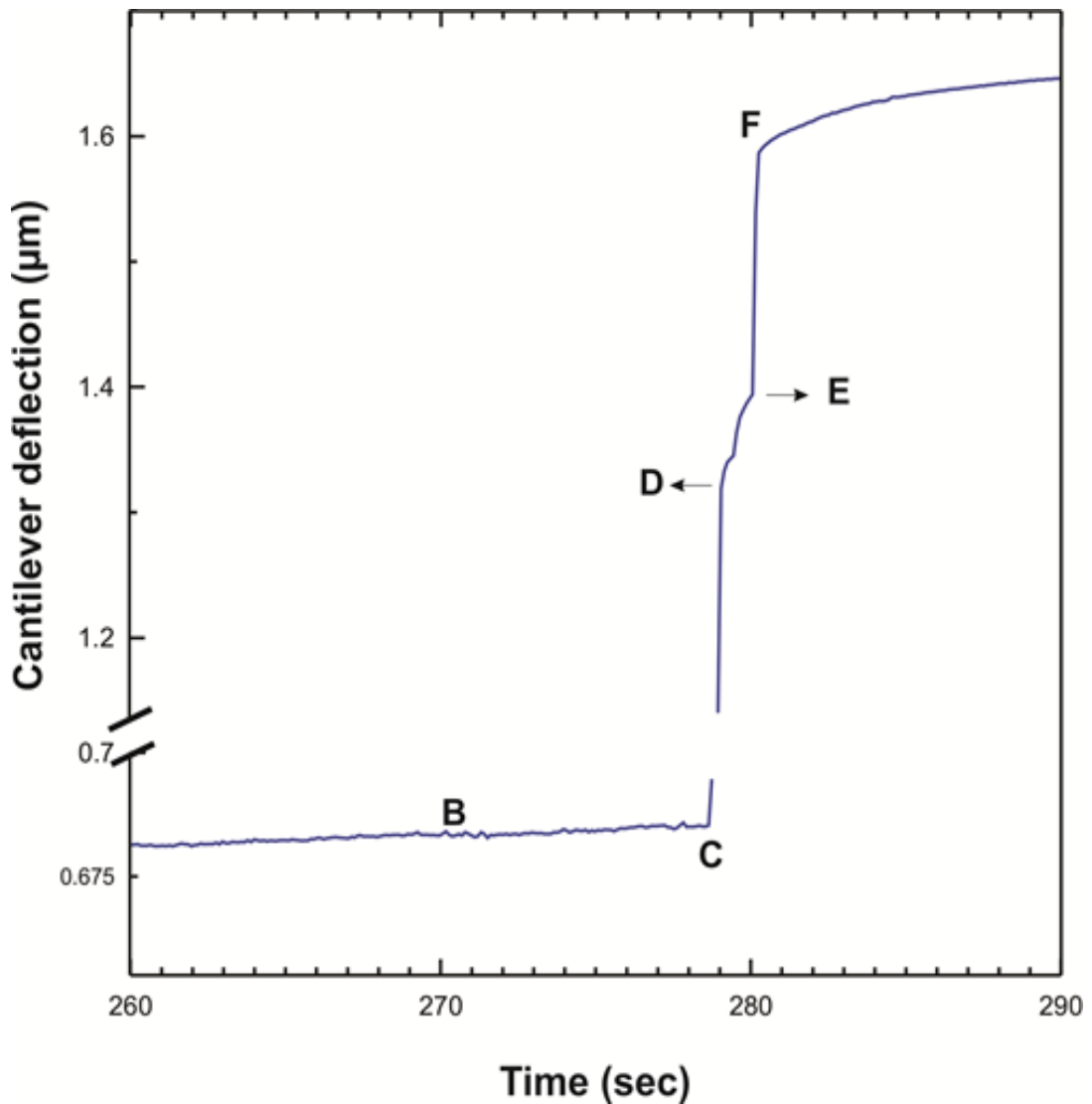


**Figure 4.7:** The cantilever deflection (in  $\mu\text{m}$ ) as a function of time in response to the process described above.

One of the remarkable differences between this experiment and the previous experiments is the magnitude of the capillary force. In the previous experiments where the humidity was 24 %, the capillary force acting on the cantilever at the snap-in contact point was approximately 2.4 nN, but when the humidity increased to 27 % and the separation distance between the STM tip and the cantilever at the snap-in contact point was 6 Å the magnitude of the capillary force increased to  $17 \pm 2$  nN.

The change in the relative humidity and the separation distance between the STM tip and the cantilever caused a large increase in the magnitude of the capillary force. In addition, the location where the STM tip acted on the cantilever in this experiment ( $P = 308 \pm 5 \mu\text{m}$ ) affected the response of the cantilever. When the STM tip is closer to the free end of the cantilever, the cantilever shows a higher deflection compared to the deflection if the STM tip is close to the cantilever base. The forces acting on the cantilever at  $308 \mu\text{m}$  from the cantilever base caused a large cantilever deflection which resulted in a decrease in the separation between the STM tip and the cantilever to  $6\text{\AA}$ .

#### **4.2.4 Fourth Experiment**

For this experiment, a different tip with a radius of  $128 \pm 5 \text{ nm}$  and a cantilever with spring constant of  $0.020 \pm 0.002 \text{ N/m}$  were used. The STM tip was positioned at  $210 \pm 5 \mu\text{m}$  from the cantilever base. The experiment was conducted at a relative humidity of 31%. Under this condition, an  $8 \pm 3 \text{ nm}$  thick water layer was formed on the cantilever surface [53]. Figure 4.8 shows the movement of the piezo scanner, the associated change in the tunnelling current, and the cantilever deflection recorded during the experiment. The start of the approach is indicated by point **A** in figure 4.8.

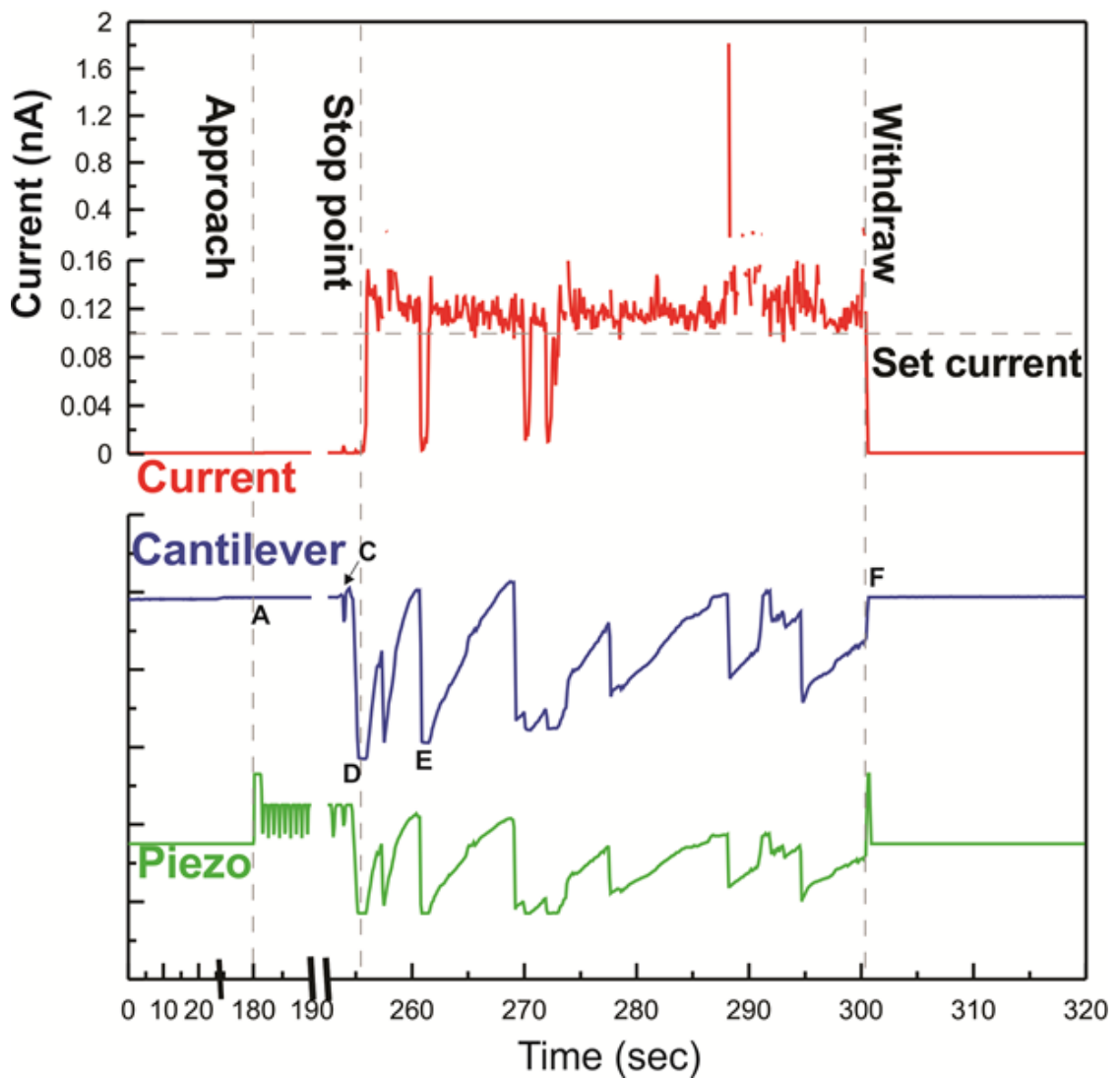


**Figure 4.8:** Measurements of the tunneling current (red), PSD signal (blue) and motion of the piezoelectric tube in the scanner (green) in response to the approach and withdrawal of the STM tip.

At point **B**, the cantilever deflected downward when the tip was close to the surface of the water layer which was speculated to be a result of the charge/neutral system interaction [40]. The cantilever deflection in  $\mu\text{m}$  units is shown in figure 4.9. When the attractive forces were strong enough to attract the cantilever, the cantilever snapped into contact with the tip (see point **C** in figure 4.9). The cantilever deflection

at point **C** was caused by attractive forces and found to be  $4 \pm 1$  nN. The STM tip radius at a separation distance of 8 nm would induce a van der Waals force of  $0.034 \pm 0.004$  nN.

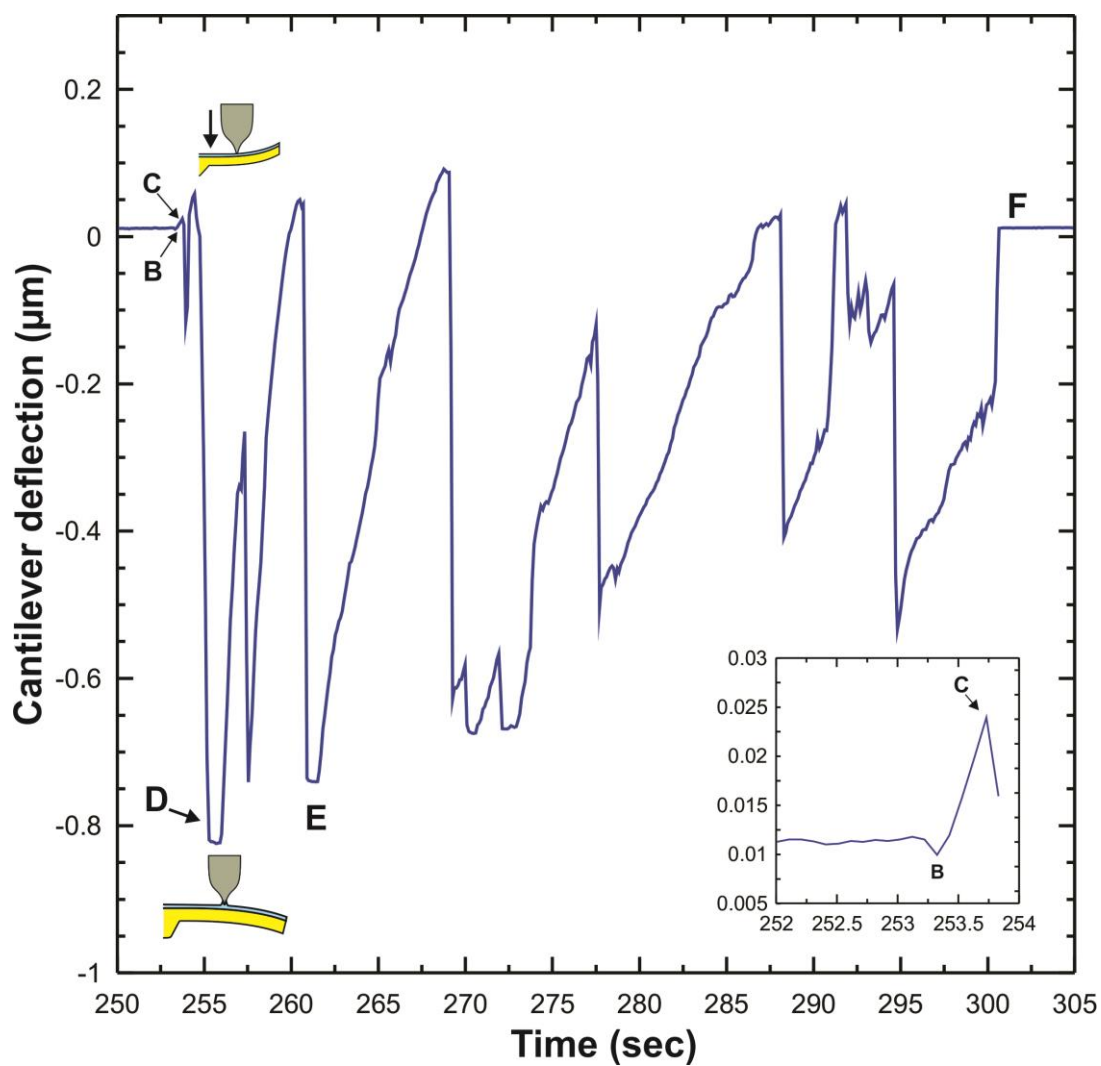


**Figure 4.9:** The cantilever deflection (in  $\mu\text{m}$ ) as a function of time. The insert is a magnified portion of the cantilever deflection at points B and C.

The capillary force was calculated by using equation 2.13, and was found to be  $5 \pm 1$  nN. Compared to the previous experiment, the small radius of the STM tip used in this experiment and the separation distance of 8 nm resulted in a small capillary force

even though the water layer thickness in this experiment was higher than the water layer thickness in the previous experiments. The calculated total attractive force ( $5 \pm 1$  nN) was slightly larger than the measured force ( $4 \pm 1$  nN) by 1 nN but within experimental uncertainties. A possible reason for this difference is that the determination of the thickness of the adsorbed water on the cantilever surface influenced the calculation of the van der Waals and capillary forces. The tip used in this experiment had a smaller radius than the tip used in the previous experiments. Because the tunnelling current is affected by the radius of the tip, the tip had to get closer to the cantilever surface to reach the tunnelling set point leading to a strong repulsive force to equilibrate the attractive forces at point **D**. The distance between the STM tip and the cantilever at point **D** was estimated to be  $6 \text{ \AA}$ . The van der Waals and capillary forces at this separation distance were approximated to be  $7.0 \pm 0.7$  and  $15 \pm 4$  nN respectively. From the deflection at point **D**, the cantilever force was found to be  $62 \pm 11$  nN. Because the net force at **D** should be zero, the repulsive was equivalent to the sum of the van der Waals, capillary and the cantilever forces, and was found to be  $84 \pm 16$  nN.

As observed in the first experiment the current went to zero at point **E** even though the piezo was fully elongated. As previously mentioned, a definite explanation has not been reached yet.

Even though the humidity was high, the cantilever was not adhered to the tip when the tip was withdrawn (point **F** figure 4.8). A possible explanation is that before the withdrawal process occurred the piezo was pulling the tip away from the cantilever to maintain the tunnelling current set point which caused the height of the water on the

tip to decrease. Therefore, the strength of the adhesive forces was decreased leading to a smooth detachment between the tip and the cantilever.

#### **4.2.5 Fifth Experiment**

An additional experiment was conducted under a relative humidity of 23%. At this relative humidity the height of the water layer on the cantilever was approximated to be  $4 \pm 1$  nm [53]. The STM tip used in this experiment had a radius of  $102 \pm 5$  nm, which was 20 nm smaller than the radius of the tip used in the previous experiment. The STM tip was located at  $219 \pm 5$  micrometer from the cantilever base. The approaching process was started at point **A** as illustrated in figure 4.10. When the STM tip came close to the water layer on the cantilever surface, the cantilever deflected downward (see point **B** in figure 4.11). This phenomenon is believed to be a result of a long range repulsive force raised from the interaction between a charged STM tip and naturally charged cantilever [40]. As demonstrated in figure 4.11, the cantilever deflected upward at point **C**, when the attractive forces were strong enough to make the STM tip snap into contact with the cantilever. Using the deflection magnitude and the location of the STM tip on the cantilever, the attractive force was found to be  $3.1 \pm 0.1$  nN. Substituting the approximate tip-cantilever separation (4 nm) and the STM tip properties into equation 2.6, the van der Waals force was found to be  $0.30 \pm 0.01$  nN. The capillary force acting on the cantilever at point **C** was found to be  $3.2 \pm 0.8$  nN. The calculated total attractive force ( $3.5 \pm 0.8$  nN) was in a close agreement with the experimentally measured force ( $3.1 \pm 0.1$  nN).

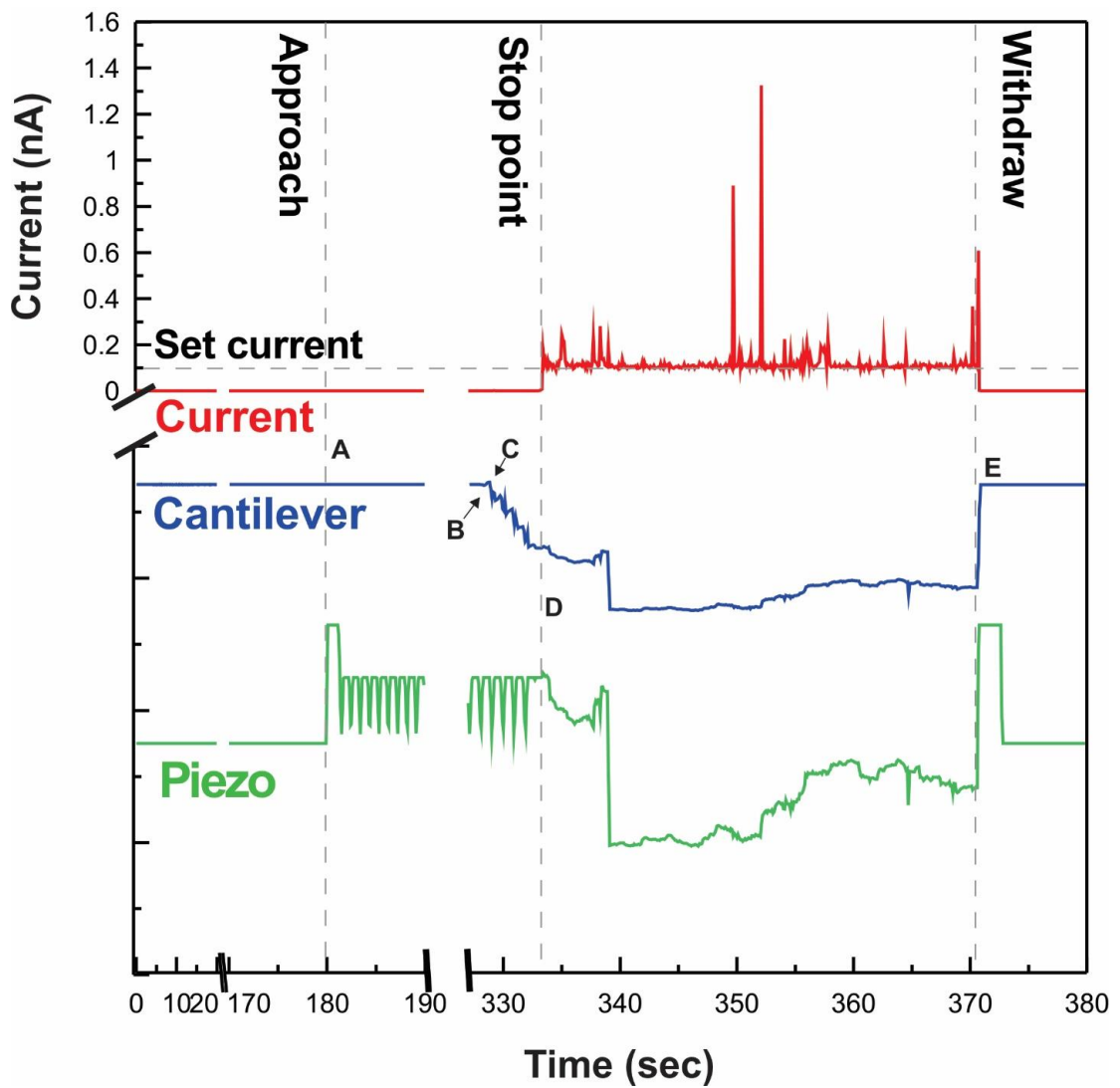


**Figure 4.10:** The changes in the tunneling current (red), PSD signal (blue) and the piezo motion (green) as a function of time when the tip was approaching, engaged and withdrawing from the Au-coated cantilever surface.

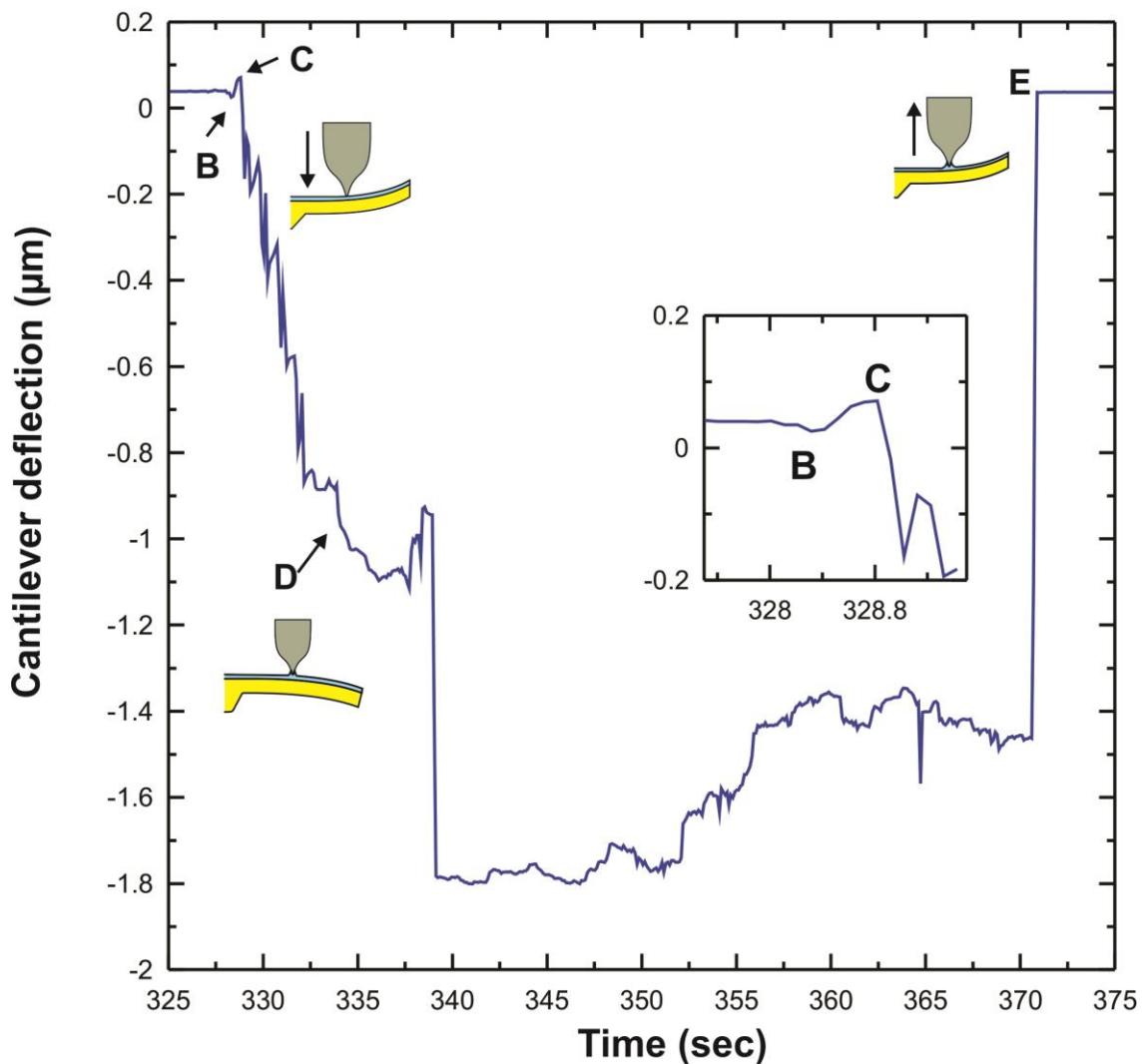


**Figure 4.11:** The cantilever deflection as a function of time in response to the STM tip. The insert is a magnified portion of the cantilever deflection at points B and C.

Compared to the previous experiment, the location of the point load on the cantilever was roughly the same. It is important to note that it is extremely difficult to adjust the location of the STM tip on the cantilever manually in order to have the same location in these experiments. In addition, the difference between the radius of the tips used in the current and the previous experiments was approximately 28 nm. It was not possible to have the same tip radius for both tips since they were commercial electrochemically etched tips. Even with this small difference in the radius of the tips

used in the current and previous experiments, the effect of the relative humidity on the interactions between the STM tip and the cantilever can be noticed.

When the tunneling current set point was reached, the approaching process stopped at point **D** as shown in figure 4.10. Since the repulsive force was acting on the cantilever at point **D** the cantilever deflected downward. The deflection of the cantilever at point **D** shows that the cantilever force acting against the repulsive force was  $62 \pm 9$  nN. The distance between the STM tip and the cantilever at point **D** was estimated to be  $6.5 \text{ \AA}$ . Therefore, the van der Waals and the capillary force at point **D** were estimated to be  $3.8 \pm 0.2$  and  $14 \pm 2$  nN respectively. The repulsive force acting on the cantilever at point **D** should be equivalent to the sum of the van der Waals, capillary and the cantilever force which was found to be  $80 \pm 10$  nN. In the previous experiment, the capillary force ( $15 \pm 4$  nN) was larger than the current experiment which was expected since the relative humidity affects the strength of the capillary force.

Before the withdraw was initiated at point **E**, the piezo was retracting and pulling the STM tip away from the cantilever to maintain the set tunnelling current. Therefore, we believed that this resulted in a smooth detachment between the STM tip and cantilever at point **E**.

The experiments show that the interaction between the STM tip and the cantilever are influenced by the relative humidity and the location of the STM tip on the cantilever. The strength of the interaction varies with the relative humidity, and the response of the cantilever depends on the strength of the forces and the location of the tip on the cantilever. The obtained results from the above experiments is presented in table 4.1.

**Table 4.1: Summary of the results that obtained from the above experiments.**

	Tip radius (nm)	Relative Humidity	Tip location ( $\mu\text{m}$ )	Snap into contact point			
				Experimentally	Theoretically		
				Total attractive forces (nN)	VDW force (nN)	Capillary force (nN)	Total attractive forces (nN)
<b>First experiment</b>	216 $\pm$ 14	24%	260 $\pm$ 5	2.4 $\pm$ 0.5	0.16 $\pm$ 0.04	2.22 $\pm$ 0.4	2.4 $\pm$ 0.4
<b>Second experiment</b>	216 $\pm$ 14	24%	280 $\pm$ 5	2.8 $\pm$ 0.4	0.16 $\pm$ 0.04	2.20 $\pm$ 0.2	2.4 $\pm$ 0.2
<b>Third experiment</b>	216 $\pm$ 14	27%	308 $\pm$ 5	27 $\pm$ 2	11.2 $\pm$ 0.8	17 $\pm$ 3	29 $\pm$ 4
<b>Fourth experiment</b>	128 $\pm$ 5	31%	210 $\pm$ 5	4 $\pm$ 1	0.034 $\pm$ 0.004	5 $\pm$ 1	5 $\pm$ 1
<b>Fifth experiment</b>	102 $\pm$ 5	23%	219 $\pm$ 5	3.1 $\pm$ 0.1	0.3 $\pm$ 0.01	3.2 $\pm$ 0.8	3.5 $\pm$ 0.8

# Chapter 5 Conclusion and future work

## 5.1 Conclusion

In this work, we have investigated the interactions between a Pt/Ir STM tip and a Au coated cantilever under ambient conditions. Our goal was to understand why it was not possible to perform STM imaging on cantilever sensors when the distance of the STM tip from the cantilever base increased. In order to achieve this goal, a new experimental setup was developed to study the interaction forces between a Au-coated cantilever and an STM tip.

Our experimental results showed that forces such as van der Waals, capillary and repulsive forces dominated the interactions and affected the stability of the cantilever during the interaction with the STM tip. During the experiments, the piezo oscillated up and down to maintain the tunnelling current set point. As a result, the separation distance between the tip and the cantilever changed continuously causing the magnitude of the forces to vary. The cantilever deflected up and down correspondingly due to the variation of the magnitude of the total force acting on the cantilever similarly to a forced oscillator. The deflection of the cantilever during the interaction was strongly affected by the STM tip location on the cantilever. As the

distance of the STM tip from the cantilever base increased, the cantilever deflection increased correspondingly. Unlike the set tunneling current in the fourth and the fifth experiments, the set tunneling current was poorly maintained when the tip was located closer to the free end of the cantilever as in the first, second and the third experiments. This means the instability condition of the cantilever increased and made imaging the cantilever not possible. Beside the position of the tip on the cantilever, several factors affected the strength of the interactions between the STM tip and the cantilever such as the relative humidity and correspondingly the water layer thickness on the surface of the cantilever.

The results obtained in this work showed an overall good agreement with the theoretical predictions of the forces. In the first experiment conducted under a relative humidity of 24% and with a tip radius of  $216 \pm 14$  nm at located at  $260 \pm 5$   $\mu\text{m}$  on the cantilever, the theoretical calculations predicted an attractive force of  $(2.4 \pm 0.4$  nN) whereas the experimental result gave  $(2.4 \pm 0.5$  nN). The second experiment conducted under the same conditions but with the tip located at  $280 \pm 5$   $\mu\text{m}$  on the cantilever led to a theoretically predicted attractive force of  $(2.4 \pm 0.4$  nN) whereas the experimental result gave  $(2.8 \pm 0.4$  nN) again in excellent agreement. The difference between these two results is due to where the tip was located in the second experiment. During the third experiment, the relative humidity was 27% and the STM tip was located at  $308 \pm 5$   $\mu\text{m}$  from the edge of the chip. The experimental result showed an attractive force of  $(27 \pm 2$  nN) while the theoretical calculations gave a force of  $(29 \pm 4$  nN) also within the uncertainties. In the fourth experiment, the theoretical calculation for the attractive force for an STM tip with  $128 \pm 5$  nm radius acting on the cantilever at  $210 \pm 5$   $\mu\text{m}$  under a relative humidity of 31% was  $(5 \pm 1$

nN). The experimental results gave a force of  $(4 \pm 1 \text{ nN})$  acting on the cantilever which is 1 nN smaller than the theoretical prediction but within the experimental error. In the fifth experiment conducted under a relative humidity of 23% with a tip radius of  $102 \pm 5 \text{ nm}$  located at  $219 \pm 5 \mu\text{m}$  on the cantilever a theoretical predicted attractive force was calculated to be  $(3.5 \pm 0.8 \text{ nN})$  whereas the experimental result gave  $(3.1 \pm 0.1 \text{ nN})$  again in excellent agreement.

## **5.2 Future work**

A possible suggestion for future work is to conduct these experiments in a UHV chamber. Unfortunately, we do not have a UHV system in our laboratories. Because the capillary force is the main contributor to the interactions between the STM tip and the cantilever under ambient conditions, conducting these experiments in a controlled humidity environment would give the advantage of performing all the experiments under the same conditions which should lead to more precise measurements relating to the main objective of the study. Another possible way to eliminate the capillary force is to modify the experimental setup to incorporate a liquid cell and perform the experiments in liquids.

The results shown in Chapter 4 indicated a small repulsive force between the STM tip and the AFM cantilever immediately before the cantilever jumped in to contact with the STM tip. We believe that this repulsive force originates from interactions resulting

from a charged tip and naturally charged cantilever interaction. Future work could involve attempting to model this force by using the DLVO model.

A potential future work may also investigate the pull-off force during the withdrawal process such as observing how the contact time and the speed of the withdrawal would affect the pull-off force.

Future work should also include performing SEM imaging of the STM tip after the experiments to insure that the tip is still in a good condition and that there is no deformation of the tip resulting from the interactions.

# Bibliography

- 1- Sharpe, William N. *Springer handbook of experimental solid mechanics*. Springer Science & Business Media, 2008.
- 2- Thundat, T., Oden, P. I., & Warmack, R. J. (1997). Microcantilever sensors. *Microscale Thermophysical Engineering*, *1*(3), 185-199.
- 3- Lang, H. P., & Gerber, C. (2008). Microcantilever sensors. In *STM and AFM studies on (bio) molecular systems: unravelling the nanoworld* (pp. 1-27). Springer Berlin Heidelberg.
- 4- Lavrik, N. V., Sepaniak, M. J., & Datskos, P. G. (2004). Cantilever transducers as a platform for chemical and biological sensors. *Review of scientific instruments*, *75*(7), 2229-2253.
- 5- Adams, T. M., & Layton, R. A. (2009). *Introductory MEMS: fabrication and applications* (Vol. 70). Springer Science & Business Media.
- 6- Waggoner, P. S., & Craighead, H. G. (2007). Micro-and nanomechanical sensors for environmental, chemical, and biological detection. *Lab on a Chip*, *7*(10), 1238-1255.
- 7- Sattler, K. D. (Ed.). (2010). *Handbook of nanophysics: nanomedicine and nanorobotics*. CRC press.
- 8- Lacey, J., Stevens, R., & Beaulieu, L. Y. (2009). Scanning tunneling microscopy imaging of Au coated microcantilevers. *Journal of Applied Physics*, *105*(4), 044508.

- 9- C. J. Chen. Introduction to Scanning Tunneling Microscopy. First Edition, Oxford University Press, New York (1993)
- 10- G. Binnig, H. Rohrer (1986). "Scanning tunneling microscopy". IBM Journal of Research and Development 30: 4
- 11- Ed. R. Wiesendanger and H.-J. Guntherodt. Scanning Tunneling Microscopy I, II,III. Springer-Verlag (1993)
- 12- Kubby, J. A., & Boland, J. J. (1996). Scanning tunneling microscopy of semiconductor surfaces. *Surface science reports*, 26(3), 61-204.
- 13- Wandelt, K. (2012). *Surface and Interface Science, Volumes 1 and 2: Volume 1-Concepts and Methods; Volume 2-Properties of Elemental Surfaces* (Vol. 1). John Wiley & Sons.
- 14- Van de Leemput, L. E. C., & Van Kempen, H. (1992). *Scanning tunnelling microscopy*. Reports on Progress in Physics, 55(8), 1165.
- 15- Benedek, G. (Ed.). (2012). *Surface properties of layered structures* (Vol. 16). Springer Science & Business Media.
- 16- Sarid, D. (1994). *Scanning force microscopy: with applications to electric, magnetic, and atomic forces* (Vol. 5). Oxford University Press on Demand.
- 17- Dürig, U., Gimzewski, J. K., & Pohl, D. W. (1986). Experimental observation of forces acting during scanning tunneling microscopy. *Physical review letters*, 57(19), 2403.

- 18- Bach, C. E., Giesen, M., Ibach, H., & Einstein, T. L. (1997). Stress relief in reconstruction. *Physical review letters*, *78*(22), 4225.
- 19- Narushima, T., Kinahan, N. T., & Boland, J. J. (2007). Simultaneous scanning tunneling microscopy and stress measurements to elucidate the origins of surface forces. *Review of scientific instruments*, *78*(5), 053903.
- 20- Blanc, N., Brugger, J., De Rooij, N. F., & Dürig, U. (1996). Scanning force microscopy in the dynamic mode using microfabricated capacitive sensors. *Journal of Vacuum Science & Technology B*, *14*(2), 901-905.
- 21- Meyer, E., Hug, H. J., & Bennewitz, R. (2004). *Scanning probe microscopy: the lab on a tip*. Springer Science & Business Media.
- 22- Foster, A., & Hofer, W. A. (2006). *Scanning probe microscopy: atomic scale engineering by forces and currents*. Springer Science & Business Media.
- 23- Chen, C. J. (2008). *Introduction to scanning tunneling microscopy*. Oxford University Press.
- 24- Dedkov, G. V., Dedkova, E. G., Tegaev, R. I., & Khokonov, K. B. (2008). Measuring van der Waals and electrostatic forces for an atomic force microscope probe contacting with metal surfaces. *Technical Physics Letters*, *34*(1), 17-21.
- 25- Hiemenz, P. C., & Rajagopalan, R. (Eds.). (1997). *Principles of Colloid and Surface Chemistry, revised and expanded* (Vol. 14). CRC press.

- 26- Derjaguin, B. V., Rabinovich, Y. I., & Churaev, N. V. (1978). Direct measurement of molecular forces.
- 27- Colchero, J., Gil, A., & Baró, A. M. (2001). Resolution enhancement and improved data interpretation in electrostatic force microscopy. *Physical Review B*, **64**(24), 245403.
- 28- Law, B. M., & Rieutord, F. (2002). Electrostatic forces in atomic force microscopy. *Physical Review B*, **66**(3), 035402.
- 29- Woodward, J. T., & Zasadzinski, J. A. (1994). Height amplifications of scanning tunneling microscopy images in air. *Langmuir*, **10**(5), 1340-1344.
- 30- Butt, H. J., Cappella, B., & Kappl, M. (2005). Force measurements with the atomic force microscope: Technique, interpretation and applications. *Surface science reports*, **59**(1), 1-152.
- 31- Riedo, E., Lévy, F., & Brune, H. (2002). Kinetics of capillary condensation in nanoscopic sliding friction. *Physical review letters*, **88**(18), 185505.
- 32- Saint Jean, M., Hudlet, S., Guthmann, C., & Berger, J. (1999). Van der Waals and capacitive forces in atomic force microscopies. *Journal of applied physics*, **86**(9), 5245-5248.
- 33- Seo, Y., & Jhe, W. (2008). Atomic force microscopy and spectroscopy. *Reports on Progress in Physics*, **71**(1), 016101.
- 34- Kuchin, I. V., Matar, O. K., Craster, R. V., & Starov, V. M. (2014). Influence of the disjoining pressure on the equilibrium interfacial profile in transition zone between a thin film and a capillary meniscus. *Colloids and Interface Science Communications*, **1**, 18-22.
- 35- Hirasaki, G. J. (1991). Wettability: fundamentals and surface forces. SPE Formation Evaluation, **6**(02), 217-226.

- 36- Ho, W. W., & Sirkar, K. K. (Eds.). (1992). *Membrane handbook*. Springer Science & Business Media.
- 37- Israelachvili, J. N. (2011). *Intermolecular and surface forces: revised third edition*. Academic press.
- 38- Trefalt, G., Ruiz-Cabello, F. J. M., & Borkovec, M. (2014). Interaction Forces, Heteroaggregation, and Deposition Involving Charged Colloidal Particles. *The Journal of Physical Chemistry B*, *118*(23), 6346-6355.
- 39- Markovich, T., Andelman, D., & Podgornik, R. (2016). Charge regulation: A generalized boundary condition?. *EPL (Europhysics Letters)*, *113*(2), 26004.
- 40- Johnson, K. L., Kendall, K., & Roberts, A. D. (1971, September). Surface energy and the contact of elastic solids. In *Proceedings of the Royal Society of London A: Mathematical, Physical and Engineering Sciences* (Vol. 324, No. 1558, pp. 301-313). The Royal Society.
- 41- Derjaguin, B. V., Muller, V. M., & Toporov, Y. P. (1975). Effect of contact deformations on the adhesion of particles. *Journal of Colloid and interface science*, *53*(2), 314-326.
- 42- Dillard, D., Pocius, A., & Chaudhury, M. (2002). *Adhesion science and engineering*. (1st ed.). Amsterdam ; London: Elsevier.
- 43- Grierson, D. S., Flater, E. E., & Carpick, R. W. (2005). Accounting for the JKR–DMT transition in adhesion and friction measurements with atomic force microscopy. *Journal of adhesion science and technology*, *19*(3-5), 291-311.
- 44- Bowen, W. R., & Hilal, N. (2009). *Atomic force microscopy in process engineering: an introduction to AFM for improved processes and products*. Butterworth-Heinemann.
- 45- Shi, X., & Zhao, Y. P. (2004). Comparison of various adhesion contact theories and the influence of dimensionless load parameter. *Journal of Adhesion Science and Technology*, *18*(1), 55-68.
- 46- Girifalco, L. A., & Good, R. J. (1957). A theory for the estimation of surface and interfacial energies. I. Derivation and application to interfacial tension. *The Journal of Physical Chemistry*, *61*(7), 904-909.
- 47- Kwok, D. Y., & Neumann, A. W. (1999). Contact angle measurement and contact angle interpretation. *Advances in colloid and interface science*, *81*(3), 167-249.

- 48- Mikhelson, I., & Hicks, T. (2013). *Structural engineering formulas*. McGraw Hill Professional.
- 49- Xu, M., Tian, Y., Coates, M. L., & Beaulieu, L. Y. (2009). Measuring the cantilever-position-sensitive detector distance and cantilever curvature for cantilever sensor applications. *Review of Scientific Instruments*, *80*(9), 095114.
- 50- Beaulieu, L. Y., Godin, M., Laroche, O., Tabard-Cossa, V., & Grütter, P. (2007). A complete analysis of the laser beam deflection systems used in cantilever-based systems. *Ultramicroscopy*, *107*(4), 422-430.
- 51- Cleveland, J. P., Manne, S., Bocek, D., & Hansma, P. K. (1993). A nondestructive method for determining the spring constant of cantilevers for scanning force microscopy. *Review of Scientific Instruments*, *64*(2), 403-405.
- 52- Meyer, E. R. N. S. T. (1992). Atomic force microscopy. *Progress in surface science*, *41*(1), 3-49.
- 53- Freund, J., Halbritter, J., & Hörber, J. K. H. (1999). How dry are dried samples? Water adsorption measured by STM. *Microscopy research and technique*, *44* (5), 327-338.
- 54- Cappella, B., & Dietler, G. (1999). Force-distance curves by atomic force microscopy. *Surface science reports*, *34*(1), 1-104.